AFRL-AFOSR-VA-TR-2020-0058

Hybrid Graphene/Semiconductor Plasmonic Nano-transceiver and Nano-antenna for Terahertz-band Communication

Josep Jornet
RESEARCH FOUNDATION OF STATE UNIVERSITY OF NEW YORK THE

01/19/2020
Final Report

DISTRIBUTION A: Distribution approved for public release.

Air Force Research Laboratory
AF Office Of Scientific Research (AFOSR)/ RTA1
Arlington, Virginia 22203
Air Force Materiel Command

REPORT DOCUMENTATION PAGE

Form Approved
OMB No. 0704-0188

1. REPORT DATE *(DD-MM-YYYY)*
12-06-2020

2. REPORT TYPE
Final Performance

3. DATES COVERED *(From - To)*
01 Sep 2016 to 31 Aug 2019

4. TITLE AND SUBTITLE
Hybrid Graphene/Semiconductor Plasmonic Nano-transceiver and Nano-antenna for Terahertz-band Communication

5a. CONTRACT NUMBER

5b. GRANT NUMBER
FA9550-16-1-0188

5c. PROGRAM ELEMENT NUMBER
61102F

6. AUTHOR(S)
Josep Jornet, David Bird, Erik Einarsson, Gregory Aizin

5d. PROJECT NUMBER

5e. TASK NUMBER

5f. WORK UNIT NUMBER

7. PERFORMING ORGANIZATION NAME(S) AND ADDRESS(ES)
RESEARCH FOUNDATION OF STATE UNIVERSITY OF NEW YORK THE
402 CROFTS HALL
BUFFALO, NY 142600001 US

8. PERFORMING ORGANIZATION REPORT NUMBER

9. SPONSORING/MONITORING AGENCY NAME(S) AND ADDRESS(ES)
AF Office of Scientific Research
875 N. Randolph St. Room 3112
Arlington, VA 22203

10. SPONSOR/MONITOR'S ACRONYM(S)
AFRL/AFOSR RTA1

11. SPONSOR/MONITOR'S REPORT NUMBER(S)
AFRL-AFOSR-VA-TR-2020-0058

12. DISTRIBUTION/AVAILABILITY STATEMENT
A DISTRIBUTION UNLIMITED: PB Public Release

13. SUPPLEMENTARY NOTES

14. ABSTRACT
Terahertz-band (0.1 to 10 THz) communication is envisioned as a potential key wireless
technology to satisfy the need for much higher wireless data rates. During this project 28 refereed papers were produced from fundamental studies of THz technology for communications.

15. SUBJECT TERMS
THz, plasmon, communication technology, HEMT

16. SECURITY CLASSIFICATION OF: a. REPORT	b. ABSTRACT	c. THIS PAGE	17. LIMITATION OF ABSTRACT	18. NUMBER OF PAGES	19a. NAME OF RESPONSIBLE PERSON
Unclassified	Unclassified	Unclassified	UU		GORETTA, KENNETH
					19b. TELEPHONE NUMBER *(Include area code)* 703-696-7349

Standard Form 298 (Rev. 8/98)
Prescribed by ANSI Std. Z39.18

Hybrid Graphene/Semiconductor Plasmonic Nano-transceiver and Nano-antenna for Terahertz-band Communication:

Final Performance Report

Josep Miquel Jornet[1], Erik Einarsson[1], Gregory Aizin[2] and Jonathan P. Bird[1]

[1] Department of Electrical Engineering
University at Buffalo, The State University of New York
Buffalo, NY 14260, USA
Email: {jmjornet,erikeina,jbird}@buffalo.edu

[2] Department of Physical Sciences
Kingsborough Community College
Brooklyn, NY 11235, USA
Email: gaizin@kingsborough.edu

Reporting Period: September 2016–August 2019

Contents

Hybrid Graphene/Semiconductor Plasmonic Nano-transceiver and Nano-antenna for Terahertz-band Communication:

Final Performance Report

Josep Miquel Jornet, Erik Einarsson, Gregory Aizin and Jonathan P. Bird

1 Introduction

1.1 Terahertz Communications and their Relevance to the U.S. Air Force

Over the last few years, wireless data traffic has drastically increased due to a change in the way today's society creates, shares and consumes information. At the end of 2017, the need to provide wireless connectivity to *anything*, *anywhere*, *anytime* resulted in more than 8.6 billion mobile devices connected to the Internet, which generated a total of 11.5 exabytes per month of mobile data traffic [1]. Moreover, estimates forecast that there will be 12.3 billion mobile-connected devices by 2022, in part due to the Internet of Things paradigm. In parallel to the growth in the total number of interconnected devices, there has been an increasing demand for higher speed wireless communication. In particular, wireless data rates have doubled every eighteen months for the last three decades [2]. Following this trend, *Terabit-per-second (Tbps) links* are expected to become a reality within the next five years.

Several alternatives are being considered to meet this demand. *At frequencies below 5 GHz*, advanced digital modulations and sophisticated physical layer schemes are being used to achieve a very high spectral efficiency. However, the very small bandwidth available in the overcrowded electromagnetic (EM) spectrum limits the achievable data rates. For example, in LTE-A Pro networks, peak data rates in excess of 3 Gigabit-per-second (Gbps) are feasible by means of multi-carrier aggregation (up to 32x20 MHz) when utilizing a 8x8 MIMO scheme [3]. Similarly, dynamic spectrum access and sharing techniques are being heavily investigated to better utilize the available bandwidth. While these technologies will contribute to achieve maximum spectral efficiency, they are far from being able to support Tbps.

Millimeter-wave (mm-wave) communication systems (30 to 300 GHz) have gained a lot of attention in the last few years due to their ability to support much higher data rates than communication systems below 5 GHz [4]. Several sub-bands have been allocated for communications, including 38.6 to 40 GHz (1.4 GHz bandwidth), 57 to 64 GHz (7 GHz bandwidth, but usually smaller due to international regulations) and 71 to 76 GHz/81 to 86 GHz (10 GHz bandwidth in total). Millimeter-wave technology is already playing a key role in current (e.g., IEEE 802.11ad) wireless systems, and will continue to do so in future (e.g., 5G and beyond cellular) systems. While on the right track, the total consecutive available bandwidth for mm-wave communication systems is still less than 10 GHz. Supporting Tbps would require a physical layer efficiency of almost 100 bit/s/Hz, which is several times higher than the state of the art for existing systems.

Optical wireless communication systems, operating in the infrared (187 to 400 THz/ 750 to 1600 nm), visible (400 to 770 THz/390 to 750 nm), or even ultraviolet (1000 to 1500 THz/200 to 280 nm) EM spectrum bands, are similarly being explored as a way to improve the achievable data rates in wireless networks [5]. The intrinsically very large available bandwidth at such very high frequency plays to their advantage. However, there are several aspects that currently limit these approaches and require further research, including the size and limited portability of infrared systems, low transmission power budget due to eye-safety limits and the impact of atmospheric effects on the signal propagation (e.g., scattering from molecules and particles), or the impact of ambient noise in visible communication.

In this context, ***Terahertz-band (0.1 to 10 THz) communication*** **is envisioned as a potential key wireless technology to satisfy the need for much higher wireless data rates [6–9].** The THz band supports huge transmission bandwidths, which range from almost 10 THz for distances below one meter, to multiple transmission windows, each tens to hundreds of GHz wide, for distances on the order of a few tens of meters. Nevertheless, this very large bandwidth comes at the cost of a very high propagation loss [10]. For many decades, the lack of compact high-power signal sources and high-sensitivity detectors able to work at room temperature has hampered the use of the THz band for any application beyond sensing. However, many recent advancements with different technologies is finally closing the so-called THz gap.

Independently of the specific enabling technology, **THz-band communication can address three relevant challenges for the U.S. Air Force.** First, THz-band frequencies (0.1 to 10 THz) remain almost completely unutilized for communication; hence, being the first to exploit this band provides an unmatched technological advantage. Second, the very high propagation loss at THz frequencies can be leveraged to create intrinsically secure air-to-air communication channels [11]. On the one hand, the high spreading loss requires the utilization of ultra-directional systems, which enable ultra-low PI/PD communications. On the other hand, atmospheric absorption at THz-band frequencies drastically limits the ability to intercept or disrupt air-to-air communications from ground systems, thus, further enhancing the security of the air-to-air links. Third, the THz band supports huge transmission bandwidths (from hundreds of GHz up to a few THz, depending on the transmission distance and medium composition). This can enable, for the first time, wireless Terabit-per-second (Tbps) links and opens the door to transformative applications, such as in-air big-data sharing for real-time monitoring, decision and actuation with unmanned aerial vehicle networks. Ultimately, THz communications will contribute to realizing the vision of the Air Force Future Operating Concept [12] by *diversifying the portfolio of capabilities needed to achieve operational agility.*

1.2 State of the Art in Terahertz Technology

For many decades, the lack of compact high-power signal sources and high-sensitivity detectors able to work at room temperature has hampered the use of the THz band for any application beyond sensing. However, many recent advancements with several device technologies [13] are finally closing the so-called THz gap. In an *electronic approach*, the limits of standard silicon CMOS technology [14], silicon-germanium BiCMOS technology [15], III-V semiconductor HEMT [16], mHEMT [17], HBT [18], and Schottky diode [19] technologies are being pushed to reach the 1 THz mark. These systems commonly rely on frequency-multiplying chains to up-convert a multi-GHz local oscillator to THz frequencies. Power loss due to the generation of non-desired harmonics and limited gain of these devices when approaching true THz frequencies hamper the energy efficiency and limit the feasibility of this approach for higher frequencies. In a *photonics approach*, uni-traveling carrier photodiodes [20], photoconductive antennas [21], optical downconversion systems [22] and quantum cascade lasers [23] are being investigated for high-power THz systems. The latter can yield THz emission across a broad spectrum, offering output in the range of tens of milliwatts at cryogenic temperatures. However, they suffer from poor performance at room temperature.

A promising alternative to realizing THz communications is to leverage the properties of plasmonic materials to develop THz transceivers and antennas. Among others, a III–V semiconductor-based HEMT-like structure, with a 2D electron gas (2DEG) channel that is formed at a high-quality heterointerface, can be utilized to electrically excite 2D plasmons at THz frequencies. In particular, when a dc current is passed through the HEMT channel, spontaneously excited plasmons drift with the 2D electron fluid. The electron drift causes the Doppler shift in the plasmon dispersion. Plasmon reflection from the channel boundaries reverses the Doppler shift and may result in the amplification of the plasma wave amplitude. Dyakonov and Shur [24] have shown that if the plasmon reflection conditions at the opposite ends of the channel (the drain and the source boundaries) are asymmetric, the instability may be developed when the amplitude of the plasma wave increases exponentially, provided that the plasma wave gain exceeds the damping losses –the Dyakonov-Shur (DS) instability. In the non-linear regime, the plasmonic system is stabilized due to the electromagnetic (EM) radiation at the plasmon frequency in the THz range. In this process, the kinetic energy of the drifting plasmon is transformed into EM energy.

This DS instability has been studied numerically and experimentally in a number of publications [25–29]. For typical HEMT parameters, the frequency of the unstable plasma modes lies in the THz range, and significant effort has focused on implementing a THz transmitter based on this effect [30]. However, these efforts have been largely unsuccessful because the EM power radiated into free space has proved to be too weak for practical use [28, 30]. One of the main reasons behind this problem is the complexity introduced when creating the asymmetric boundary conditions in the HEMT. Since its original inception by Dyakonov and Shur, it has been considered that the source impedance approaches zero ohm, and the drain impedance tends to infinity, something which practically cannot be assumed. Similarly, in a wireless communication system, the need to attach the source to a modulator or ultimately an antenna, will further modify such impedance. As a way to circumvent these limitations, the use of plasmonic nanomaterials such as graphene has been considered [31–33]. Among many other relevant properties, graphene supports the propagation of surface plasmon polariton (SPP) waves at THz-band frequencies. This is a very unique property, as SPP waves only propagate in metals in the infra-red and above. In addition, the SPP wave properties can be dynamically tuned by changing the graphene conductivity, which ultimately leads to reconfigurable devices.

1.3 Our Approach and Contributions

Motivated by these properties, our group advocates for the development of hybrid graphene/semiconductor plasmonic devices for THz-band communications. In this direction, we also proposed and numerically analyzed an on-chip THz plasmonic signal source based on a hybrid graphene III–V semiconductor HEMT [34]. Compared to existing plasmonic sources, the generated plasma wave is not directly radiated, but utilized to launch an SPP wave on the graphene layer that extends towards the antenna. In order to efficiently radiate the generated SPP wave, in [35, 36], we proposed and numerically analyzed for the first time the use of graphene to build plasmonic nano-antennas that can be tuned to efficiently operate in the THz band. The proposed nano-antennas, which leverage the propagation properties of SPP waves on graphene, are just a few micrometers in their largest dimension, thus can be easily integrated with plasma wave devices. More recently, in [37], we proposed a way to modulate the phase of a SPP wave as it propagates from the source to the antenna, in order to enable robust phase modulation schemes for communications.

Starting from our preliminary results, the **objective of this project** has been to model, fabricate, and characterize an integrated system capable of sourcing THz signals on demand and propagating these on- and off-chip for high-speed wireless communication, all by leveraging the properties of hybrid graphene/semiconductor heterostructures. During this three-year-long project, we have made contributions along the following two thrusts:

- **Hybrid Graphene/semiconductor Plasmonic On-chip Terahertz Source:** We have analytically modeled the DS instability in real-world structures, by taking into account the impact of non-ideal termination impedances at the source and the drain as well as the connection of the antenna, all by utilizing different approaches (from the transmission line model to the hydrodynamic equations) [38, 39]; we have developed a multi-physics simulation platform that self-consistently solves the hydrodynamic model equations with Maxwell's equations in the time domain, and utilized that platform to obtain accurate results that guide the experimental fabrication and device design [40]; we have proposed and developed a technique to control the termination impedances at the source and drain of the HEMT, so to create the required asymmetric boundary conditions, and we have repeatedly fabricated and electrically characterized the fabricated devices [41].

- **Graphene-based Plasmonic Nano-antenna Arrays:** We have proposed, designed and analytically and numerically modeled graphene-based plasmonic nano-antenna arrays in the presence of mutual coupling, in transmission and reception [42–44]; we have also investigated the design and control of hybrid graphene/metal reflect-array antennas, which can be utilized to enhance the propagation of THz signals [45, 46]; we have developed a method to fabricate and transfer large graphene samples, and we have patterned the graphene structures according to different antenna and antenna arrays designs [47]; we have developed and made extensive use of 2D material characterization techniques based on THz time-domain spectroscopy [48–50]; and we have experimentally tested our developed (reflect) arrays [51, 52].

In the following sections, we summarize the progress in these two main thrusts for each year of the project.

2 Year 1

2.1 Hybrid Graphene/semiconductor Plasmonic On-chip Terahertz Source

The focus in Year was on the development of the fundamental analytical models for the DS instability in two Coulomb-coupled 2DEG layers with real antenna as a demonstration of principle. In addition, we identified ways to experimentally create the required asymmetry between the source and the drain impedances and started the fabrication process.

2.1.1 Transmission Line Model of the Dyakonov-Shur Instability

The focus of this task was on the modeling of the plasmon propagation and the DS plasma instability [24] in the dc biased 2D electron channel of the HEMT gated by the graphene sheet instead of the metal. Since the graphene sheet represents another 2D electron conducting layer the unstable plasmons in the HEMT channel excite the plasmons of the same frequency in the graphene. The latter plasmons channeled into the graphene based nano-antenna should produce electromagnetic radiation of the THz frequency.

From the theoretical standpoint, the problem reduces to the study of the plasmon propagation in the two Coulomb-coupled parallel 2D electron layers separated by the dielectric barrier of thickness d. To generate the DS instability one of the layers should be biased and carry a dc current characterized by the constant electron drift velocity v_{dr} [24]. Another 2D layer is connected to the radiating antenna with the radiation resistance R_{ANT}. This double 2D electron layer system has finite length L ($L \gg d$). Asymmetric boundary conditions at the source (x=0) and the drain (x=L) are crucial for the generation of the DS instability [24]. The asymmetry is provided by the different terminating impedances at the source and the drain of the double-layer structure. These impedances describe the capacitive coupling between both layers (Z_{12}) and between the layers and the adjacent contacts (Z_1). Schematic diagram of the considered model system is shown in Fig. 1.

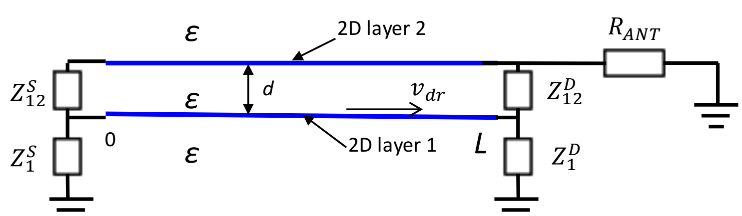

Fig. 1: Schematic diagram of the model double 2D layer THz source.

The Dyakonov-Shur instability in the double 2D electron layer with antenna In the first step, we assumed the ideal boundary conditions with zero terminating impedances at the source ($Z_1^S = Z_{12}^S = 0$) and infinite terminating impedances at the drain ($Z_1^D = Z_{12}^D = \infty$). To check the validity of the suggested model we also assumed that both layers are formed in the semiconductor structure where electrons are described by the effective mass $m*$ and quadratic dispersion law.

Plasma excitations in the interacting electron system are well described by the hydrodynamic model [53]. In this model, it is assumed that the time of electron-electron collisions is much smaller than any other characteristic time scale. Under such condition, the electron system reaches local thermodynamic equilibrium in every point and is characterized by the macroscopic local velocity and local electron density [54]. In this approximation, the electron system behaves as a fluid and is described by the hydrodynamic equations: the Euler equation and the equation of continuity. These equations should be supplemented by the Poisson equation describing the Coulomb interaction between the charged density fluctuations within each layer and between the layers.

Solving hydrodynamic equations together with the Poisson and imposing the boundary conditions described above we obtain the following dispersion equation for the plasmon of frequency ω:

$$\left[1+\frac{v_{dr}\beta_2}{v_p}\left(i\frac{\omega L}{v_p}-2\right)\right]e^{i\frac{\omega L}{v_p}}-\left[1+\frac{v_{dr}\beta_2}{v_p}\left(i\frac{\omega L}{v_p}+2\right)\right]e^{-i\frac{\omega L}{v_p}}$$
$$+\frac{R_{ANT}}{z_0\beta_1^2}\left\{\left[1+\frac{v_{dr}\beta_2}{v_p}\left(i\frac{\omega L}{v_p}-1\right)\right]e^{i\frac{\omega L}{v_p}}+\left[1+\frac{v_{dr}\beta_2}{v_p}\left(i\frac{\omega L}{v_p}+1\right)\right]e^{-i\frac{\omega L}{v_p}}\right\}+4\beta_2\frac{v_{dr}}{v_p}=0 \tag{1}$$

Here $\beta_{1,2}=\frac{n_{01,2}}{n_{01}+n_{02}}$ are relative electron densities in the layers 1 and 2 with equilibrium electron densities n_{01} and n_{02}, respectively, $v_p=\sqrt{\frac{e^2dn_{01}n_{02}}{m*\varepsilon\varepsilon_0(n_{01}+n_{02})}}$ is an acoustic plasmon velocity in the infinitely long system, and $Z_0=\frac{d}{\varepsilon\varepsilon_0 Wv_p}$ is the characteristic impedance of the plasmonic transmission line formed by the two 2D electron layers of width W embedded into the medium with dielectric constant ε. In (1), we have also neglected the effect of the finite electron momentum relaxation time τ assuming $\omega\tau\gg 1$.

The numerical solution of (1) for both real and imaginary parts of the complex plasma frequency $\omega=\omega'+i\omega''$ as a function of the radiation resistance R_{ANT} is presented in Figs. 2a and 2b, respectively. In this calculation, we assumed $\frac{v_{dr}}{v_p}$=0.2 (red, green, and blue lines) and $v_{dr}=0$ (gray lines). The plasma frequency is quantized in the plasmonic cavity of length L formed between the source and the drain contacts. The first three levels only are shown in Fig. 2. When $R_{ANT}\to 0$, the cavity is symmetric, and plasma frequencies are given by the expression $\omega_n=\frac{\pi v_p}{L}n$, n=1,2, ... When $R_{ANT}\to\infty$, the cavity is strongly asymmetric with plasma frequencies $\omega_n=\frac{\pi v_p}{2L}(2n-1)$, n=1,2, ... The most important result is the behavior of the imaginary part of the frequency ω''. Positive ω'' implies the damping plasma wave, and negative ω'' implies the DS instability when the plasma wave amplitude exponentially increases. The results shown in Fig. 2b indicate that the DS instability develops at $R_{ANT}/Z_0\gtrsim 10$ (radiation regime). For InGaAs semiconductor nanostructures with 2D electron density $n_0=3\cdot 10^{11}$ cm^{-2}, d=20 nm, L=100 nm, and W=10 μm we have $Z_0\approx 30\Omega$, so the required R_{ANT} should be achievable experimentally. At smaller R_{ANT} the loss of energy due to antenna radiation exceeds the gain of energy by the plasma wave from the dc current, and the amplitude of the plasma wave exponentially decreases (damping regime). The maximum damping occurs at $R_{ANT}=Z_0$ when the antenna impedance is matched with the cavity impedance. It also follows from Fig. 2 that some plasma modes become unstable at very small R_{ANT}. The physical mechanism of this effect is currently unclear and requires additional analysis.

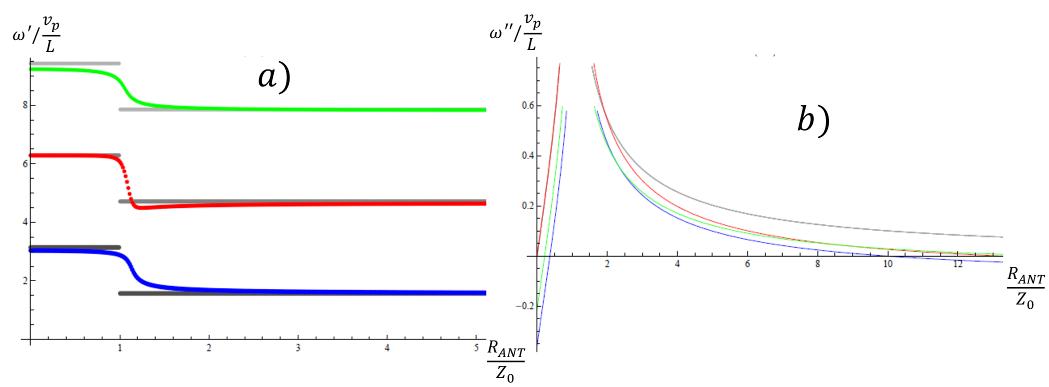

Fig. 2: Real (a) and imaginary (b) parts of the complex plasma frequencies in the double 2D electron layer in the semiconductor structure with antenna.

The instability described here was obtained in the linear approximation when the fluctuations of the electron density and velocity are small, and perturbation theory allows the analytical solution of the hydrodynamic equations. Using this approach, we were able to demonstrate the emergence of the DS instability and existence of the radiation regime in the dc biased double 2D electron layer system in the broad interval of the antenna radiation resistances exceeding some threshold value. However, the linear analysis becomes inadequate when the amplitude of the plasma oscillations increases, and the perturbation theory is not applicable. The results obtained so far should be viewed as an important demonstration-of-principle. At large plasma wave amplitudes the non-linear processes stabilize the plasma oscillations and establish the stationary radiation regime where the gain of energy from the dc current is balanced by the energy radiated by the antenna. To describe this regime the numerical solution of the non-linear hydrodynamic equations is required. This solution should include the real geometry of the system, the effect of additional plasma damping due to finite electron momentum relaxation time, and the finite values of the terminating impedances. This work is planned to be done in the next funding period.

The hydrodynamic theory of the dc current biased 2D graphene layers In the suggested THz source, one of the 2D electron layers is the graphene layer. The theory described in the previous section should be modified to include specific features of the 2D electron layer in graphene. The 2D electrons in graphene are massless Dirac fermions with linear dispersion law $\varepsilon = v_F|\boldsymbol{p}|$, where $\boldsymbol{p}$ is the electron momentum and $v_F = 1 \cdot 10^6$ m/s is the constant electron velocity [55]. The linearity of the electron spectrum should significantly modify the hydrodynamic equations describing the 2D electron fluid in graphene [56].

First, we are developing the hydrodynamic theory of the 2D electron fluid in graphene. The hydrodynamic equations can be derived by calculating the moments of the classical Boltzmann kinetic equation for the massless fermions [57]. The first moment does not depend on the specific form of the electron dispersion law and yields the standard equation of continuity for the local electron density. The second moment yields the Euler equation. For the electron fluid in graphene characterized by the local macroscopic velocity $v(x,t)$ and the local electron density $n(x,t)$ our calculations yield

$$\frac{\sqrt{\pi}\hbar}{v_F}\frac{\partial}{\partial t}\left(\frac{n^{3/2}(x,t)\,v(x,t)}{\left(1-v^2(x,t)/v_F^2\right)^{1/4}}\right)+\frac{\sqrt{\pi}\hbar v_F}{3}\frac{\partial}{\partial x}\left(\frac{n^{3/2}(x,t)\left(1+2v^2(x,t)/v_F^2\right)}{\left(1-v^2(x,t)/v_F^2\right)^{1/4}}\right)+eE(x,t)\,n(x,t)=0 \qquad (2)$$

This Euler equation together with the equation of continuity and electrodynamics equations should be used for description of the plasma collective excitations in graphene.

As the first application of the derived hydrodynamic equations we calculated the plasmon dispersion law in the gated graphene layer biased by the dc current described by the constant drift velocity v_{dr}. We assumed that the metal gate is positioned at distance d from the 2D graphene layer. The schematic diagram of this system is shown in Fig. 3.

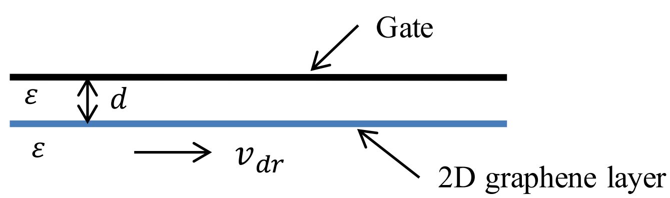

Fig. 3: Schematic diagram of the current biased gated 2D graphene layer used in the plasmon spectrum calculations.

Assuming that the gate separation d is much smaller than the plasmon wavelength we found the wave velocities of the acoustic plasmons propagating in the direction of the electron drift v_+ and in the opposite direction v_-. Dependences of the velocities v_+ and v_- on the drift velocity is shown in Fig. 4. It follows from Fig. 4 that the dependence of $v_\pm$ on v_{dr} is strongly non-linear [58]. This result is in stark contrast with the velocities of the acoustic plasmons in the gated semiconductor 2D electron layer where the constant electron drift results in the linear Doppler shift of the plasma frequency. This additional non-linearity can potentially increase the increment of the DS instability in the double 2D electron graphene layers and hybrid graphene-semiconductor systems.

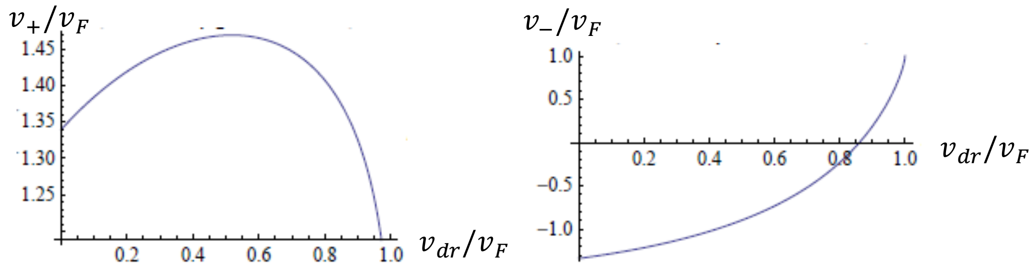

Fig. 4: Velocities of the acoustic plasmons propagating in the direction of the electron drift v_+ and in the opposite direction v_- in the gated graphene layer.

In addition to the theoretical models developed in this period, we started the development of the multi-physics numericla platform, finalized and reported in Year 2.

2.1.2 Device Fabrication: Definition of Asymmetric Boundary Conditions

In parallel to the development of the analytical and numerical models, we worked towards the fabrication and experimental characterization of the proposed structures. While there have been a number of prior experimental attempts to search for this “DS instability", these efforts have largely been fruitless, a fact that may primarily be attributed to the difficulties associated with implementing the asymmetric boundaries at the ends of the FET. It is this specific problem that we address in this study, in which we fabricate III-V (GaAs- and InAs-based) FETs in the which asymmetric boundary conditions are implemented through the inclusion of narrow, sub-micron, constrictions at one end of the channel.

The essential structure of the devices that we were fabricated in Year 1 is illustrated in Fig. 5. It should be emphasized that this ultimate design was reached after a 6-month period exploring earlier designs, whose lithography challenges and likely output power were deemed to be unacceptable for this project. The essential working principle of this device, which is implemented in a III-V heterostructure with 2DEG around 100–200 nm below its top surface, is as follows. While the device features two large ohmic contacts, either of which may function as the FET source, dependent upon the manner in which the voltage is applied to the contacts, the “drain" of the device is then connected to the channel through the etched constriction near the center. This, therefore, provides a practical realization of the asymmetric boundary conditions required for the DS instability. The instability itself is generated in the “cavity" region formed electrostatically underneath the narrow finger gates shown in the image. By positioning this cavity just a few hundred nanometers or less from the constriction, a practical implementation of the DS scheme should be realizable.

The essential element in the fabrication of the device structure in Fig. 5 is the precise alignment of the finger gate relative to the etched edge of the boundary. To this end, we have been exploring techniques for highly-selective etching of the constriction structure, and for the precise alignment of the finger gate relative to this. In Fig. 6, we show an example where we have used electron-beam lithography and dry etching to form a narrow constriction between a pair of rectangles, inside of which etching has been performed. Working in parallel with this, we have also addressed the issues associated with aligning a nanoscale-width gate relative to the edges of the etched regions, over a distance that extends to as much as a hundred microns. This should allow us to achieve the targeted device structure in the coming months.

Implementing the targeted DS instability is not simply a problem of nanofabrication, but also requires us to understand the electrical characteristics of the fabricated structures. The challenge here is to realize physical constrictions that generate a sufficient impedance mismatch with the FET source, but which nonetheless remain sufficiently conducting to support the current needed for plasmonic generation. Consequently, we have also been studying the correlation between the structural size of the nanoconstrictions and their electrical properties. An example is provided in Fig. 7, in which we show the current-voltage characteristics measured at room temperature for etched constrictions of varying physical width (indicated). These data

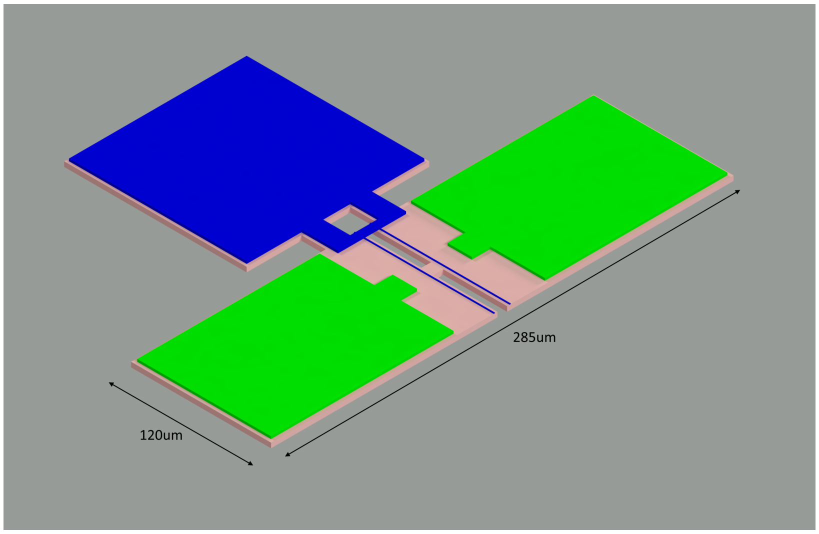

Fig. 5: Schematic illustration of a plasmonic THz source based on the DS instability.

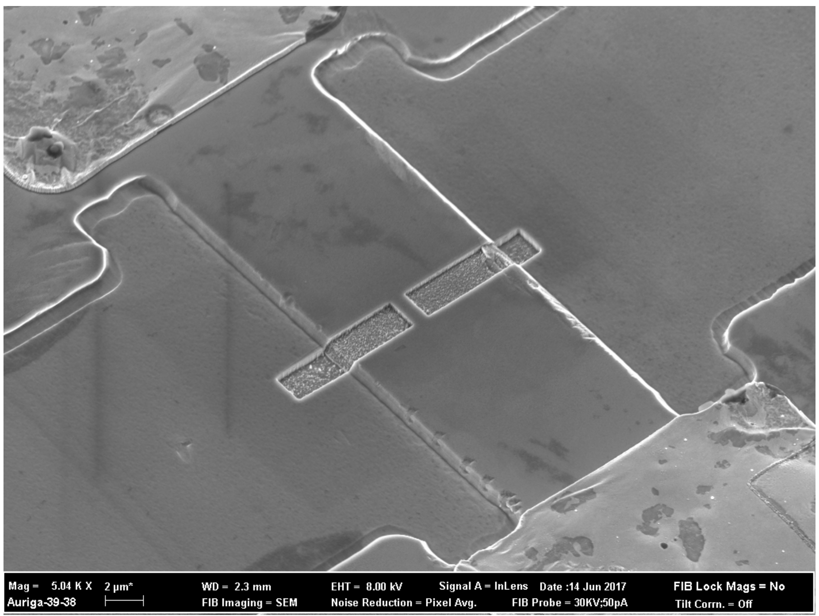

Fig. 6: Scanning electron micrograph showing an etched constriction formed in a wider mesa structure. Although not shown here, finger gates will be fabricated to run parallel to the long edge of the two etched rectangles. Note the size marker in the image which denotes a distance of 2 μm.

clearly demonstrate the capacity to manipulate physical structure to achieved desired electrical function. Overall, the different curves show significant nonlinearity which is common for structures of this kind when they are operated under nonequilibrium. We also observe a clear correlation between physical structure and channel current, which decreases systematically as the constriction width is reduced.

The various results of Figs. 5-7 demonstrate the essential elements that are needed to implement the proposed THz source. During the next funding period, we fully expect to be able to provide a practical demonstration of this functional device.

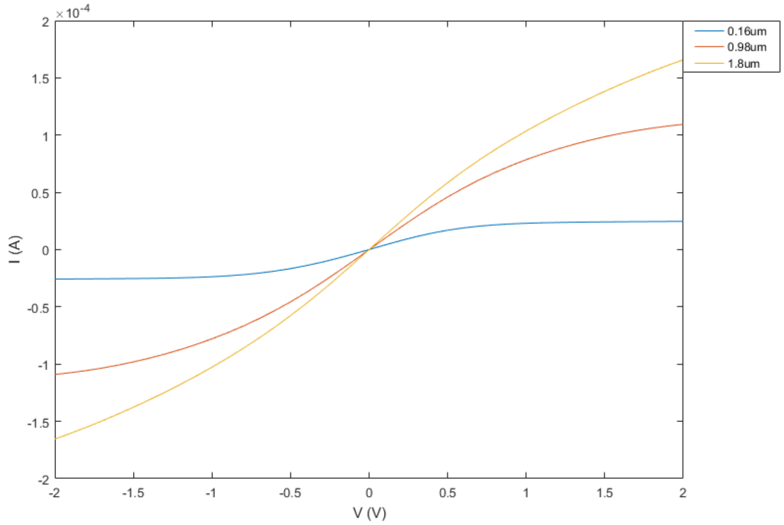

Fig. 7: Room temperature current-voltage characteristics of etched constrictions of differing width.

2.2 Graphene-based Plasmonic Nano-antenna Arrays

Graphene-based plasmonic nano-antennas can be utilized to efficiently radiate the SPP waves generated by our proposed on-chip THz source. Since our very first work in 2010 [35], there have been many studies concerning graphene antennas which investigate variations such as electrically tunable [59], reconfigurable [60], and beamforming antennas [61]. Nevertheless, there are several limitations in single-antenna systems that motivate the development of graphene-based nano-antenna arrays [62]. An array configuration would simultaneously solve some of the inherent roadblocks to THz communication while opening up many new possibilities. For one, single nano-antennas suffer from limited available output power due to their small size, which can be up to three magnitudes smaller than the size of current wireless communication antennas. In addition, the THz band itself introduces significant losses in the form of spreading losses and attenuation due to molecular absorption. A THz band array can alleviate these problems by producing huge increases in gain due to power amplification and/or beamforming. In addition, large arrays introduce the possibility to take advantage of Multiple-Input and Multiple-Output (MIMO) communication schemes for both beamforming and spatial multiplexing.

In the design of an array there are two equally important challenges. In addition to the optimization of each individual antenna element, the second challenge is to determine how these individual elements should be placed relative to each other. Here mutual coupling concerns become just as important as individual design, as this determines how closely antennas can be placed and subsequently determines the size of the total array. Some works have been done in this area, but they are not sufficient or applicable to this case. For example, in [63] coupling is considered between graphene nanoribbons, but it does not consider how the distance between elements affects coupling strength and how it impacts system performance. Analysis is needed which considers coupling among nano-antennas.

During the first year of this project, we focused on the designing, modeling, fabricating and experimentally testing such structures.

2.2.1 Plasmonic Array Design in the Presence of Mutual Coupling

As part of this task, we first analyze the mutual coupling between graphene-based nano-antennas. A mathematical analysis is provided along with numerical simulation of a two element array, which focuses on how the strength of mutual coupling changes with respect to the separation distance. The second contribution is an investigation of the performance of nano-antenna arrays in terms of the achievable gain and directivity.

In addition to the ideal gain, the impact of mutual coupling on the gain is considered. The analytical coupling model is validated by electromagnetic simulations, which is also used to simulate performance of the array.

Coupled Mode Theory The coupling between two resonant modes, such as those excited in resonant plasmonic nano-antennas, can be described mathematically using coupled mode theory. A full coupled mode model of the nano-antenna consists of a resonator with terms for conduction losses, radiation losses, and incident power from outside waves. From [63], the amplitude of the fields in two such nano-antennas is given by:

$$\frac{d\tilde{a}_1}{dt} = (i\omega_1 - \gamma_1 - \Gamma_1)\tilde{a}_1 + ik\tilde{a}_2 + i\sqrt{\gamma_1}(s_+ + i\sqrt{\gamma_2}e^{-ikd}\tilde{a}_2), \tag{3}$$

$$\frac{d\tilde{a}_2}{dt} = (i\omega_2 - \gamma_2 - \Gamma_2)\tilde{a}_2 + ik\tilde{a}_1 + i\sqrt{\gamma_2}(s_+ + i\sqrt{\gamma_1}e^{-ikd}\tilde{a}_1), \tag{4}$$

where a_1 and a_2 refer to the amplitudes and ω_1 and ω_2 are the natural frequencies [64]. In addition, γ is the radiative loss, Γ is the conduction loss, k is the coupling coefficient, s_+ is an incoming plane wave, and $\tilde{a}_{1,2} = a_{1,2}e^{j\omega t}$. While this is physically the case, when the goal is to investigate the near field coupling the model is greatly simplified by considering only the case of two lossless resonators. This is possible because the radiative and conductive losses are purely real, and therefore do not affect the resonance conditions induced by the reactive fields. In addition, when nano-antenna separation distances are small enough the near field coupling effects dominate and the coupling due to re-radiation of energy can be assumed to be zero [63]. Therefore, we assume that $\Gamma = 0$, $\gamma = 0$, and $s_+ = 0$, and that the resonators are excited by a time varying function. In this case, the equations for the resonators are given as:

$$\frac{da_1}{dt} = j\omega_1 a_1 + k_{12}a_2, \tag{5}$$

$$\frac{da_2}{dt} = j\omega_2 a_2 + k_{21}a_1. \tag{6}$$

The theory is valid as long as the coupling perturbations can be considered linear, which is true if the coupling terms $k_{12}a_2$ and $k_{21}a_1$ are much smaller than $j\omega_1 a_1$ and $j\omega_2 a_2$. Due to the symmetry of the problem, as well as energy conservation constraints discussed in [64], k_{12} must be equal to k_{21}. By taking this system of linear equations, one can solve for the eigenfrequencies, resulting in:

$$\omega = \frac{\omega_1 + \omega_2}{2} \pm \sqrt{\left(\frac{\omega_1 - \omega_2}{2}\right)^2 + |k_{12}|^2}, \tag{7}$$

where all the terms have been previously defined.

Physically the eigen-frequencies can be understood as the natural resonant frequencies of the two nano-antennas. Because a nano-antenna is a passive component, if the natural resonance frequency changes the result is not that the antenna will change operating frequency, but rather that it will now only radiate efficiently at the new resonances. In a system where the nano-antennas are already being exciting by a driving frequency, a change in the natural resonance will manifest itself as a change in the input impedance of the system. A typical array will be excited with the same frequency in each antenna. In this case, $\omega_1 = \omega_2 = \omega_0$, and the equation for the eigenfrequencies simplifies to

$$\omega = \omega_0 \pm k, \tag{8}$$

where k is the coupling coefficient, which is the result of the non-radiating near fields in the antenna. In conventional microstrip antenna theory, it is derived from Maxwell's equations. There have been multiple attempts to model the mutual coupling between elements by using the transmission line model [65], the cavity model [66] [67] [68], or the method of moments for microstrip antennas. While these studies have had success in predicting coupling in metallic microstrip antennas, they have drawbacks which limit their use in studying coupling between plasmonic nano-antenna arrays. The problem is that most studies neglect surface waves to simplify the model. In a plasmonic nano-antenna, surface waves are critical to the operation of the antenna, and in fact are the only kind of waves that can be supported [36]. Even when studies account for surface waves, these surface waves are fundamentally different from SPP waves. The surface waves on metallic antennas occur at dielectric-dielectric boundaries and propagate over the entire dielectric surface. These waves detract from the total power available to be radiated. In contrast, a plasmonic nano-antenna relies on SPP waves for generating the electric field and are only supported on the boundary between a dielectric and a metal, which means they can only exist where the patch is present. Because of these differences, the models used for predicting the coupling coefficient in metallic antenna arrays cannot be assumed to work for plasmonic arrays. Further analysis is needed which takes into account the properties of SPP waves.

Because the wavelength in a plasmonic nano-antenna is confined to a much smaller length than the radiated free space wavelength, it is expected that the mutual coupling will only start to become a major factor at distances related to the plasmonic wavelength, and consequently allow array elements to be separated much less than would be required in a perfect electric conducting antenna. Taking this into consideration, we predict that the coupling coefficient can be approximated by an exponential function given as

$$k = \alpha\omega_0 e^{-d\beta}, \tag{9}$$

where ω_0 is the resonant frequency without coupling, α and β are tuning constants, and d is the separation distance between elements.

Performance of Plasmonic Nano-antenna Arrays In the design of an array, it is important to consider the overall system performance and how it is impacted by coupling and other factors. An array constructed using graphene nano-antennas will differ in two important aspects from a conventional array. First, as previously discussed, the coupling is expected to be based mainly on the physical size of the nano-antenna. For a plasmonic nano-antenna where there is a high confinement factor, near field coupling will only be an issue at distances much less than the free space wavelength. On one hand, this will allow for array elements to be placed much closer in proximity to each other, resulting in a high density of elements in the available area. On the other hand, this limits the beamforming abilities, which require distance comparable to the free space wavelength in order to achieve constructive superposition of field amplitudes. Second, the possibility to use one plasmonic signal source per antenna to power every element individually means that an increase in output power, and consequently gain, can be achieved independently of phase variation or beamforming. These differences are illustrated by considering the array factor $\mathcal{AF}$ of a uniform square planar array with N powered elements per side, separated by a distance of λ, which is given in [69] by

$$\mathcal{AF}(\theta,\phi) = \left(\frac{\sin\left(N\frac{\psi_x}{2}\right)}{\sin\left(\frac{\psi_x}{2}\right)}\right)\left(\frac{\sin\left(N\frac{\psi_y}{2}\right)}{\sin\left(\frac{\psi_y}{2}\right)}\right), \tag{10}$$

$$\psi_x = kd\sin\theta\cos\phi - \frac{2\pi}{kd}\sin\theta_0\cos\phi_0, \tag{11}$$

$$\psi_y = kd\sin\theta\sin\phi - \frac{2\pi}{kd}\sin\theta_0\sin\phi_0, \tag{12}$$

where θ refers to the elevation angle, ϕ is the azimuth, (θ_0, ϕ_0) is the beam pointing direction, $k = \frac{2\pi}{\lambda}$ is the wavenumber, and d is the uniform distance between elements. In a conventional array $\mathcal{AF}$ is normalized with respect to N to account for the total power being split between N antennas, and to better illustrate radiation pattern changes from field multiplication. However, here it is left unnormalized with respect to N due to the fact that the nano-antennas will be powered independently and contribute to the overall gain. In addition, for a plasmonic nano-antenna array the distance between the elements will be the plasmonic

Table 1: Curve fitted Parameters for k

Frequency	1 THz	5 THz	8 THz
α	0.02563	0.02158	0.02188
β	$1e10^{-11}$	$1e10^{-11}$	$1e10^{-11}$

wavelength rather than some multiple of the freespace wavelength. In this case, we replace d with the plasmonic wavelength λ_{spp}, and the array factor becomes

$$\mathcal{AF}(\theta,\phi) = \left(\frac{\sin\left(N\frac{\psi_x}{2}\right)}{\sin\left(\frac{\psi_x}{2}\right)}\right)\left(\frac{\sin\left(N\frac{\psi_y}{2}\right)}{\sin\left(\frac{\psi_y}{2}\right)}\right), \tag{13}$$

$$\psi_x = \frac{2\pi}{\gamma}\sin\theta\cos\phi - \frac{2\pi}{\gamma}\sin\theta_0\cos\phi_0, \tag{14}$$

$$\psi_y = \frac{2\pi}{\gamma}\sin\theta\sin\phi - \frac{2\pi}{\gamma}\sin\theta_0\sin\phi_0, \tag{15}$$

where γ is the confinement factor and is equal to $\frac{\lambda}{\lambda_{\mathrm{spp}}}$. When using this formula it is clear that the higher the confinement factor becomes, the lower the directivity will be, although it still has a minimum value of 1. However, analysis using this formula suggests that even with decreased directivity due to a high confinement factor, or equivalently, close element spacing, the attainable gain is still high due to power multiplication.

Simulation and Numerical Results In this section, the analytical model for the mutual coupling coefficient is validated, and the nano-antenna array performance claims are verified by means of full-wave electromagnetic simulations. In order to numerically find the coupling coefficient, a two element array is simulated using COMSOL Multiphysics. Graphene is modeled as a transition boundary condition with complex-valued dynamic conductivity given by the model in [70], where $\tau_g = 0.5$ ps is the relaxation time of electrons in graphene, $T = 300$ K is the temperature, and with E_F values from 0.1 to 1.25 eV, where E_F is the Fermi energy of the graphene patch. These values are based on analysis of Raman spectra obtained from CVD-grown graphene. The graphene layer rests on top of a 90-nm-thick SiO_2 dielectric ($\epsilon_r = 4$), which separates the graphene from the ground plane. This thickness is chosen because it maximizes visual detection of graphene on SiO_2. The antenna is fed with a lumped port that connects the graphene layer to the ground plane on one side. A perfectly matched layer and scattering boundary are used to accurately approximate an infinite space. The antennas are meshed with a resolution of $\lambda_{spp}/5$. To simulate the array performance measures of gain and directivity, the same parameters are used to construct a uniform planar three by three array for a total of nine elements.

Validation of Mutual Coupling: The effect of mutual coupling on resonant frequency was found through the measurement of the input impedance at the ports. As previously discussed, the frequency at which the imaginary part of the input impedance disappears is considered to be the resonant frequency. The mutual coupling dependency on the separation of the elements was found by performing a frequency sweep for different separation distances for three different frequencies that are representative of the THz band. The coupling coefficient (9) was also plotted using curve fitting tools to match the tuning parameters. As shown in Fig. 8, the change in frequency as a function of separation distance is comparable to the plasmonic wavelength, which in this case is 2 μm for both simulations. It also shows that the matched coupling coefficient equations are well matched to their respective coupling sweeps. Table 1 summarizes the matched coefficients for each frequency.

Analysis of Array Performance: In addition to studying the change in frequency in a two element array, the overall array performance and the impact of mutual coupling on this performance was simulated. The simulation used a nine element array, and directivity and gain are calculated from radiated power values computed by COMSOL. The directivity as plotted in Fig. 9a takes into account the combined effects of

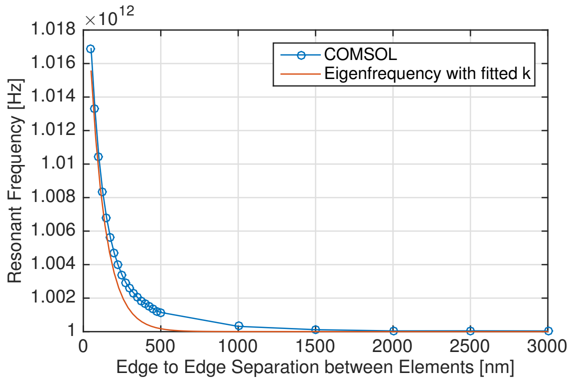

(a) 1 THz

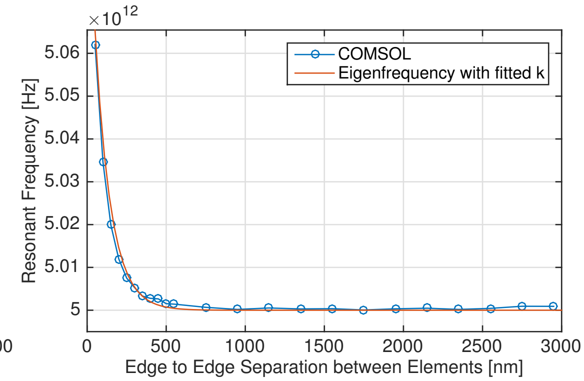

(b) 5 THz

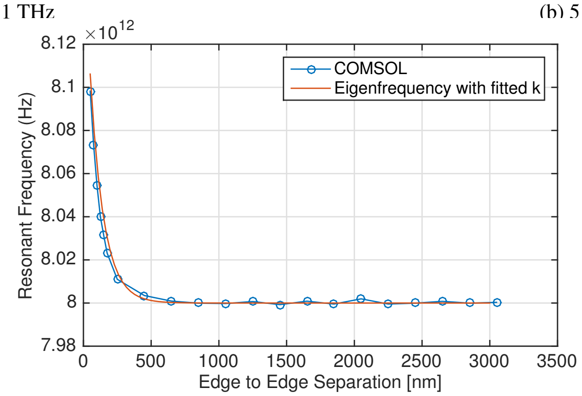

(c) 8 THz

Fig. 8: Resonance frequency as a function of the separation distance between resonant elements for different antenna resonant frequencies.

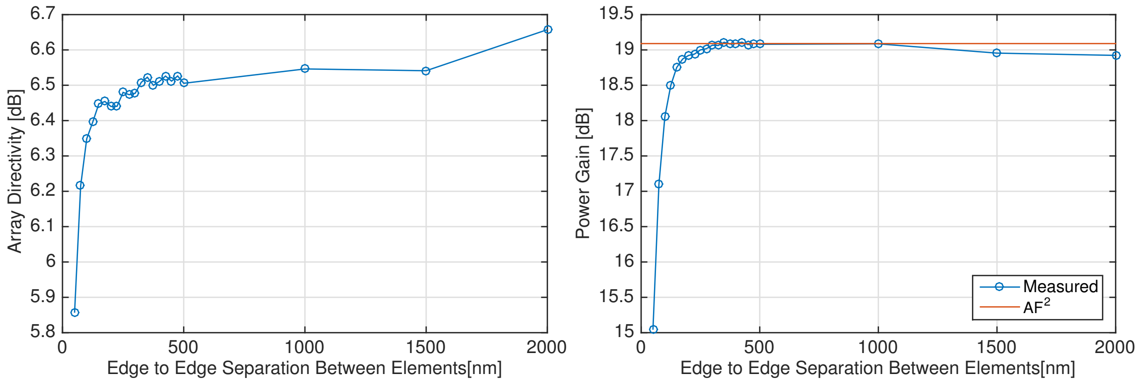

(a) Directivity

(b) Power gain

Fig. 9: Directivity and power gain of a nine antenna uniform planar array as functions of the separation between elements.

the array directivity and the single nano-antenna's directivity, while neglecting power amplification. What can be seen from the graph is that the directivity when the antenna separation distance is comparable to λ_{spp} is predominately due to the directivity of the single nano-antenna, which is about 6.5 dB. The added directivity from the array due to constructive interference does not occur until the separation approaches $\lambda/2$. In Fig. 9b, the power multiplication gain of the array over that of a single nano-antenna is plotted. This gain in power is shown to be equal in magnitude to the square of the array factor, which for an array of nine elements is equivalent to 81, or about 19 dB. In both figures it is clear that mutual coupling effects cause a large drop in both directivity and power gain, but only for very close separation distances.

Finally, in Fig. 10, the total gain of a plasmonic array is calculated based on the number of antennas in the array for different separation distances. The total gain shown here represents the maximum radiated power of a plasmonic array compared to that of a single isotropic nano-antenna and includes the directivity of a graphene nano-antenna, the directivity of the array, and the power multiplication from multiple powered antennas. It is important to note that even the lowest separation distance shown here is large enough that mutual coupling effects are not a concern.

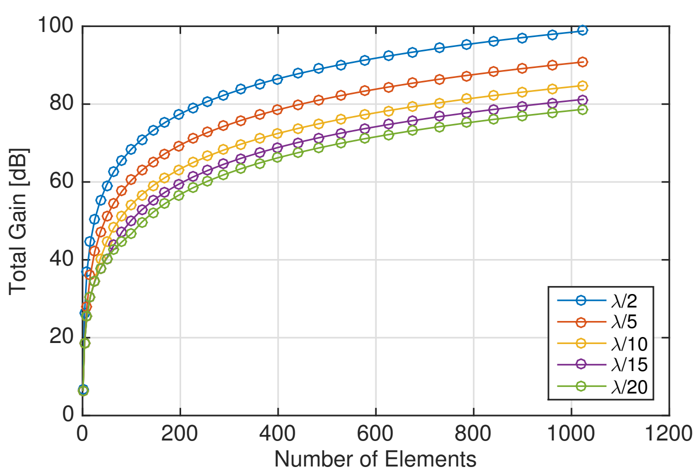

Fig. 10: Total gain of a graphene-based plasmonic nano-antenna array, as a function of the number of elements.

2.2.2 Array Fabrication and Experimental Characterization

In parallel to the development of the analytical and simulation models, we have been working towards the fabrication and experimental characterization of graphene-based plasmonic nano-antenna arrays. Next, we explain our progress within the first year.

Graphene synthesis We grow monolayer graphene using low-pressure chemical vapor deposition (LPCVD) and methane as a precursor. Before growth, we clean as-received copper (Cu) foil (Sigma-Aldrich, Lot # MKBP8380V, 25 µm thick) in acetone, isopropyl alcohol (IPA), and deionized (DI) water. We place the cleaned Cu foil on a 300 °C hot plate for 40 min to oxidize the surface. After oxidation, we place the Cu foil in the center of a 90 cm horizontal split furnace then heat the furnace to 1000 °C while continuously supplying a mixture of 5% hydrogen (H_2) in 95% nitrogen (N_2) at a flow rate of 500 sccm. After reaching the target temperature, we continue the gas flow for 60 min to anneal the Cu foil. After annealing, we synthesize graphene by introducing methane gas (99.97% purity) in three steps: 0.1 sccm for 15 min, followed by 1 sccm for 10 min, and then 10 sccm for 5 min. Throughout the growth process we maintain a system pressure of 2.4 kPa.

Graphene transfer In preparation for transfer, we spin-coat a poly(methyl methacrylate) (PMMA) solution onto the as-grown graphene film. We use a PMMA solution with molecular weight of 495 kDa and a concentration of 4% in anisole (MicroChem, 495PMMA A4). For copolymer deposition, we use a commercially available poly(methylmethacrylate/methacrylic acid) copolymer at a concentration of 9% in ethyl lactate (EL) (MicroChem, MMA(8.5)MAA EL9). After adding the first PMMA layer, we proceed with one of the following methods, which are shown diagrammatically in Fig. 11.

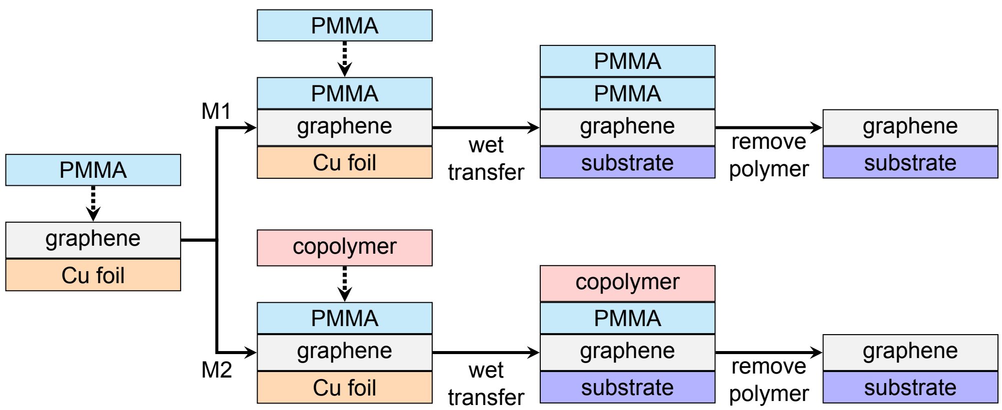

Fig. 11: Schematic diagram of graphene wet transfer. M1 and M2 denote method 1 (PMMA only) and method 2 (PMMA+copolymer) described in the text.

The two transfer methods are described as follows:

1. Method 1 (PMMA-only): We spin-coat a second layer of PMMA identical to the first, and then transfer the graphene as described below.
2. Method 2 (PMMA+copolymer): We spin-coat a copolymer film and perform a soft-bake for 3 min at 150 °C. To evaluate the influence of PMMA drying time on the resulting transfer, the copolymer layer is added at one of the following times:
   (a) Immediately after soft-baking the PMMA layer (before transfer to the silicon wafer)
   (b) After transferring the PMMA/graphene film onto the silicon wafer

In the wet transfer step (see Fig. 11), we remove any graphene or amorphous carbon from the back of the copper foil using oxygen plasma. We then etch the Cu foil by placing it in a 0.1 M solution of ammonium persulfate (Acros Organics, 98+%, UN1444). After dissolution of the Cu foil, we use a two-stage DI water bath (30 min each) to rinse the remaining polymer-supported graphene film and remove any residual Cu etchant. We then scoop the floating polymer+graphene film onto a cleaned target substrate and bake on a hot plate at 60 °C for 5 min. This is followed by an additional bake at 135 °C for 10 min to improve interfacial contact. In the final step, we remove any residual polymer by immersion in warm (55 °C hotplate) acetone overnight.

Graphene Pattern To pattern the transferred graphene, we spin-coat positive photoresists LOR 3B and S1818 respectively, then soft bake on a hotplate to dry the solvents. We expose the sample to UV light, as per standard photolithography methods, then immerse the sample in MF 319 developer to develop the pattern. We then perform O_2 plasma etching to remove unwanted residue and immerse the patterned sample under 1165 remover overnight for lift-off. Results of the graphene pattern process are shown in Fig. 12.

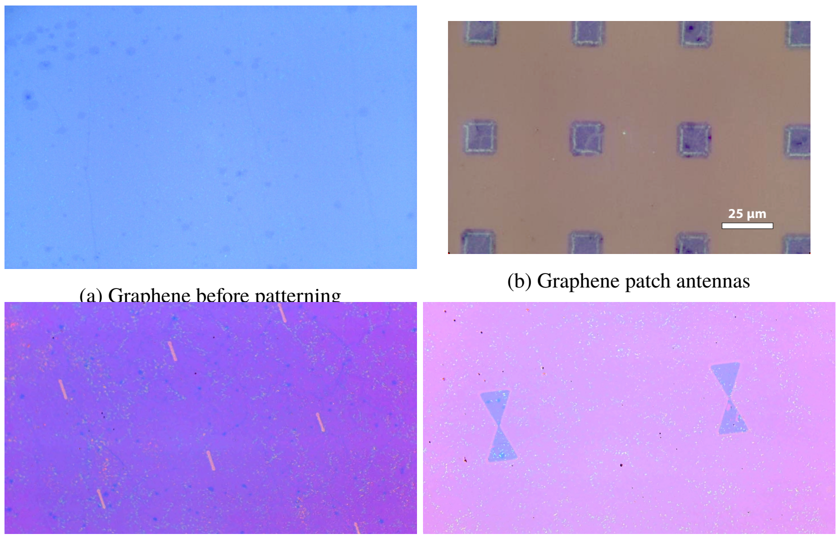

(a) Graphene before patterning

(b) Graphene patch antennas

(c) Graphene slit antennas

(d) Graphene bowtie antennas

Fig. 12: Optical micrographs of transferred graphene and subsequently patterned antenna structures.

Experimental Characterization The first preliminary step is to judge the quality of the graphene sample, which is typically done by means of Raman spectroscopy. The Raman spectrum for graphene mainly consists three peaks, shown in Fig. 13. The D peak arises from defects in graphene, the G peak comes from the

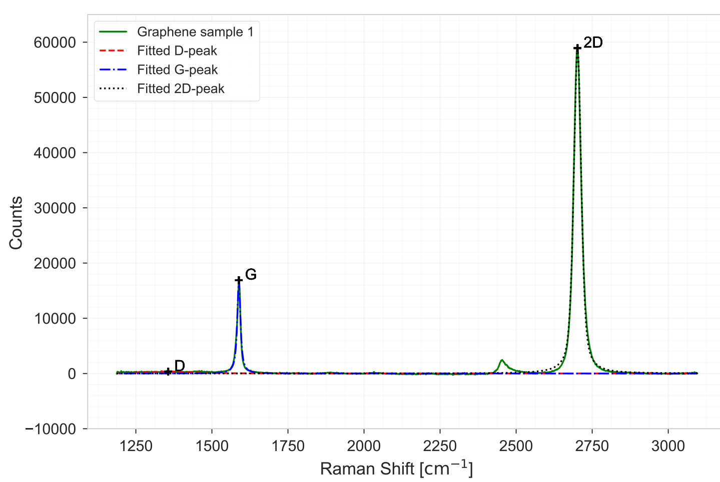

Fig. 13: Raman spectrum of graphene, with characteristic peaks indicated.

in-plane vibration of the sp^2-bonded hexagonal carbon lattice, and the 2D peak arises from an inter-valley (K-K'), double-resonant scattering process. The the number of graphene layers is typically determined from the intensity ratio of the 2D/G peaks, and the quality/crystallinity is judged by the D peak intensity. For a graphene sample with very few defects, the D/G ratio is near zero, and a 2D/G ratio greater than two indicates that the graphene is monolayer.

While Raman spectroscopy is useful in quantifying the physical quality, it reveals very little about the electrical nature of graphene. Since SPP waves only propagate where electromagnetic fields couple with electron plasma oscillations, a dielectric–conductor interface is required to excite and sustain them. Therefore, a *negative* dielectric function, which is characteristic of a conductor, becomes a defining property for a given graphene sample that could be used in plasmonic applications.

Terahertz time-domain spectroscopy (THz–TDS) is a method by which complex electrical and optical properties of a material can be extracted by probing the material with short pulses of THz light. To determine if the graphene is suitable for fabricating such plasmonic nanostructures, we use THz–TDS in reflection geometry to extract the *complex optical properties* of the transferred graphene by analyzing changes in the light–matter interaction induced by the presence of graphene on a Si/SiO_2 substrate. [48]

THz–TDS Measurement As shown in Fig. 14, a p-polarized THz pulse is incident from below on an undoped Si/SiO_2 substrate at an angle $\theta_i = 10°$. A portion of the incident pulse will be reflected from the front (main), and the rest of the signal will propagate into the substrate with a refraction angle θ_t. Some of this transmitted signal will then reflect from the back interface (echo) and exit out the front of the substrate.

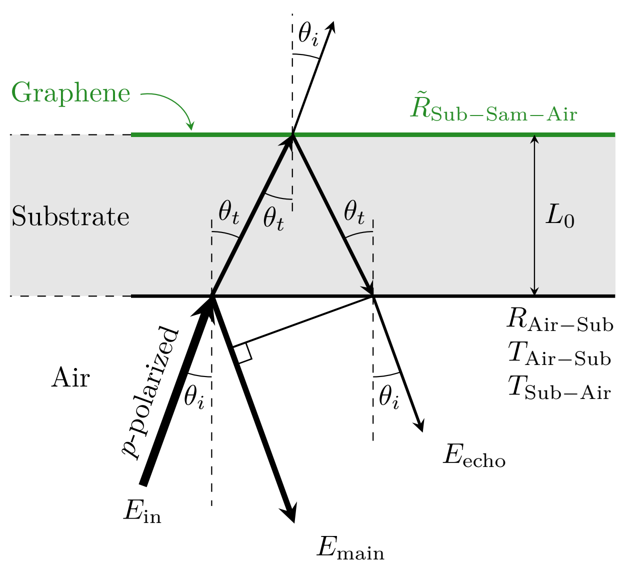

Fig. 14: Schematic of sample on substrate and THz propagation behavior at interfaces

Fig. 15 shows the time-domain THz pulse obtained from the Si/SiO_2 substrate without and with the graphene sample, respectively. We convert this time-domain signal into frequency-domain via Fourier transform to study the sample properties in the 0.5 to 2.5 THz frequency range. We then compare the electric field of the THz beam after it interacts with the sample with a reference electric field measured using a bare Si/SiO_2 substrate to extract the complex optical parameters of the sample.

Using the main pulse as the input and the echo pulse as the output, a transfer function $\tilde{H}$ is defined as follows:

$$\tilde{H} = \frac{|E_{\text{echo}}|}{|E_{\text{main}}|} \exp(-j[\phi_{\text{echo}} - \phi_{\text{main}}])$$

The substrate properties are determined via a *self-referenced* method shown below:

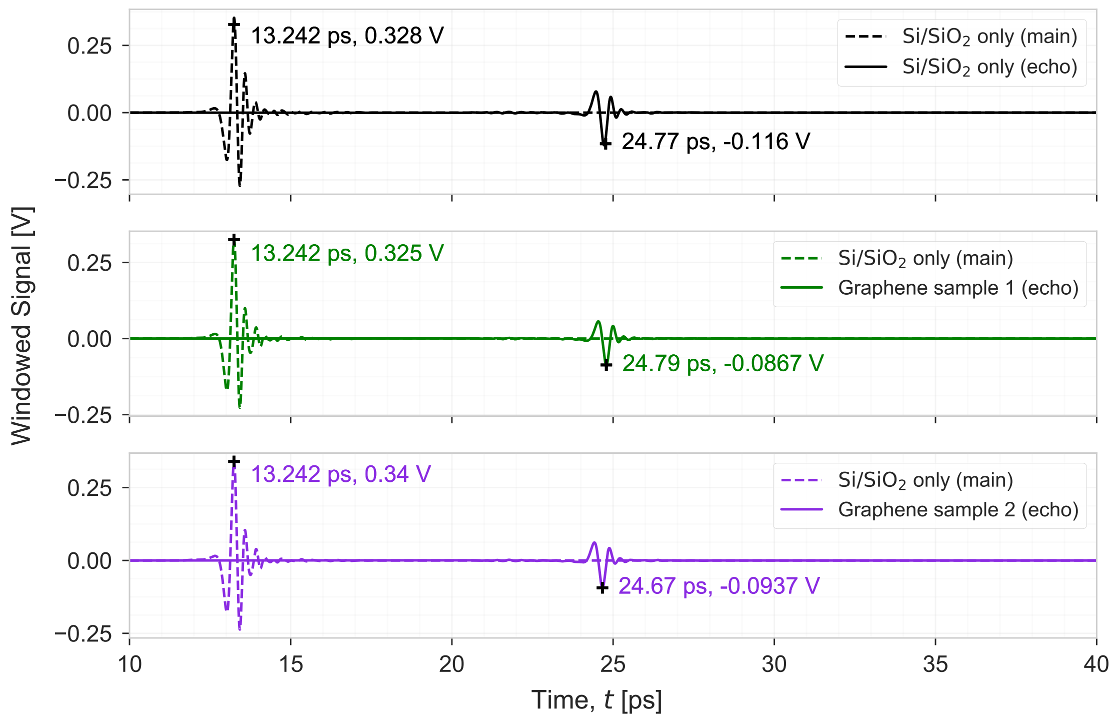

Fig. 15: THz time domain signal

- $n_{\text{Sub}} = \text{Re}[\tilde{n}_{\text{Sub}}]$, determined from the phase difference $[\phi_{\text{echo}} - \phi_{\text{main}}]$
- $\kappa_{\text{Sub}} = \text{Im}[\tilde{n}_{\text{Sub}}]$, determined from the amplitude attenuation ratio $\frac{|E_{\text{echo}}|}{|E_{\text{main}}|}$

From these two measurements, and an approach similar to that described in [71] and [72], we use the Fresnel reflection coefficient at the Si/SiO$_2$–graphene–air interface to calculate the complex conductivity of graphene using the equations given below:

$$\tilde{R}_{\text{Sub-Sam-Air}} = \tilde{H}_{\text{Sam}} \frac{R_{\text{Air-Sub}}}{T_{\text{Air-Sub}} T_{\text{Sub-Air}}} \exp\left[j \tilde{n}_{\text{Sub}} \frac{\omega L_{\text{eff}}}{c} \right]$$

$$\tilde{\sigma}(\omega) = \frac{1}{Z_0} \left[\left(\frac{1 - \tilde{R}_{\text{Sub-Sam-Air}}}{1 + \tilde{R}_{\text{Sub-Sam-Air}}} \right) \frac{\tilde{n}_{\text{Sub}}}{\cos\theta_t} - \frac{1}{\cos\theta_i} \right]$$

Kubo Formalism The electrical parameters are extracted by simultaneously fitting the real and imaginary parts of the complex conductivity by fitting it to a conductivity model. The intra-band surface conductivity of graphene is commonly modeled using the Kubo formalism given by [70],

$$\tilde{\sigma}(\omega) = \frac{A\tau}{1 - j\omega\tau}$$

where

$$A = \frac{2e^2}{\pi\hbar^2} k_B T \ln\left[2\cosh\left(\frac{E_{\text{F}}}{2k_B T} \right) \right]$$

E_{F} is the Fermi energy of graphene, and τ is the scattering time.

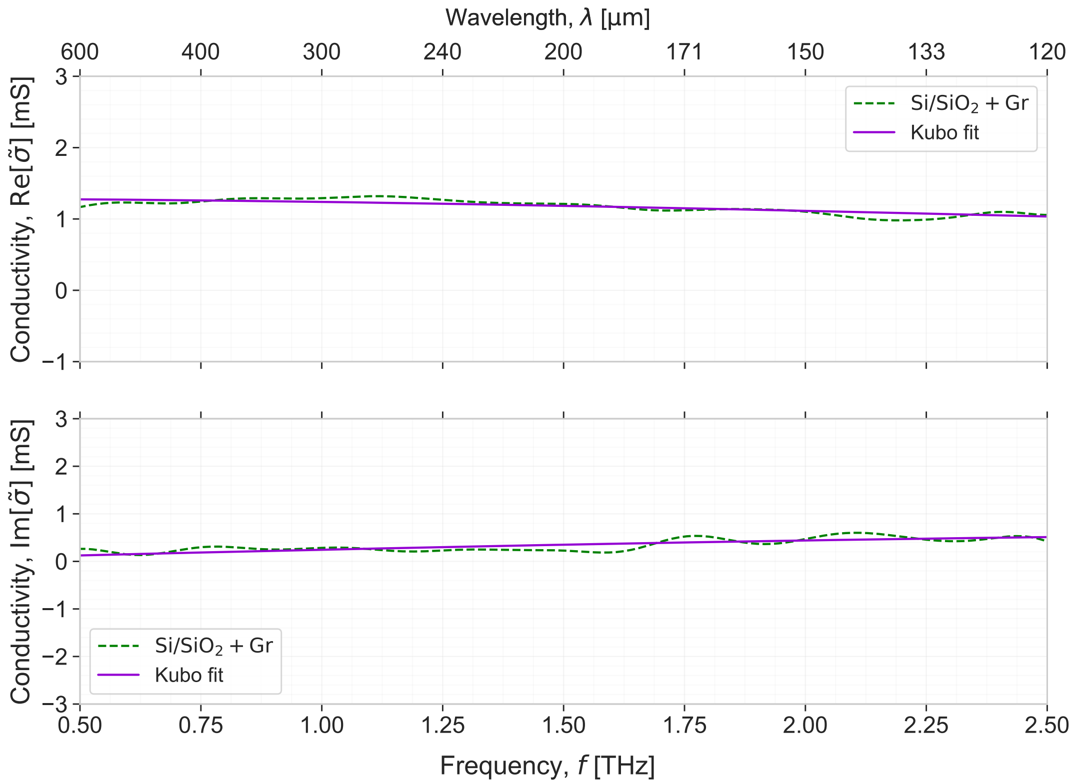

Fig. 16: Graphene complex conductivity (Kubo Model Fit)

Electrical Parameters Calculation Based on the fitted values of σ_{dc} and τ, the following parameters can be calculated as follows.

1. Fermi Energy [72]:

$$E_F = \frac{\pi \hbar^2}{e^3} \frac{\sigma_{dc}}{\tau}$$

2. Charge carrier density [73]:

$$N = \frac{\pi \hbar^2}{e^4 v_F^2} \left(\frac{\sigma_{dc}}{\tau} \right)^2$$

   where the Fermi velocity $v_F \approx 8 \times 10^5$ m/s

3. Charge carrier mobility [73]:

$$\mu = \frac{\sigma_{dc}}{eN}$$

We verified the Kubo formalism fit with the Drude and Drude-Smith models [74] typically used to fit complex conductivity of metal and metallic materials, and found them all to be in agreement as evidenced in Table 2.

In the next funding period, we are going to refine our analytical and numerical designs based on the extracted parameters, and proceed with the fabrication and patterning of the revised structure.

Table 2: Electrical parameter comparison for all models

Parameters	Drude–Smith	Drude	Kubo
Electrical conductivity, σ_{dc} [mS]	1.297	1.288	1.288
Scattering time, τ [fs]	31.66	31.45	31.45
Fermi energy, E_{F} [eV]	0.35	0.35	0.35
Carrier density, N [1/cm^2]	1.4×10^{13}	1.4×10^{13}	1.4×10^{13}
Carrier mobility, μ [cm^2/(V s)]	577.2	576.2	576.2
Backscattering parameter, c	–0.007	N/A	N/A
Goodness of fit, R^2	0.975	0.975	0.975

3 Year 2

3.1 Hybrid Graphene/semiconductor Plasmonic On-chip Terahertz Source

In Year 2, we extended our analytical models to account for the impact of non-ideal termination impedances at the source and drain of the HEMT. Then, we developed a multi-physics simulation platform that self-consistently solves the HDM equations and Maxwell's equation and utilized it to study the DS instability in HEMT with non-ideal boundary conditions and analyzed its dependence on various parameters as well as the accompanying THz radiation. In addition, we advanced the device fabrication and performed the initial electrical characterization.

3.1.1 Study of the Impact of Real Termination Impedances

Basic Equations Collective plasma excitations in the two-dimensional 2DEG in the HEMT conduction channel with a DC electric current can be described by the hydrodynamic model [53]. In this model, the 2DEG is characterized by the local electron density $n(\mathbf{r},t)$ and velocity $v(\mathbf{r},t)$ obeying the Euler and continuity equations. For a plasmon propagating in the x direction in the 2DEG layer positioned in the plane $z = 0$ these equations are:

$$\frac{\partial v}{\partial t} + v\frac{\partial v}{\partial x} = -\frac{e}{m_e^*}E_x - \frac{1}{nm_e^*}\frac{\partial P}{\partial x} - \frac{v}{\tau}, \tag{16}$$

$$\frac{\partial n}{\partial t} + \frac{\partial (nv)}{\partial x} = 0. \tag{17}$$

Here, P stands for the local pressure in the 2D electron fluid, E_x is the x component of the self-consistent electric field in the channel and $-e$ and m_e^* are the electron charge and effective mass, respectively. A phenomenological damping term included into the Euler equation in Eq. (16) accounts for the collisional damping of the plasmon with the characteristic relaxation time τ. At typical electron densities, the 2DEG in the HEMT channel remains degenerate in the broad range of temperatures up to the room temperature. In the degenerate limit, the 2D electron pressure P in Eq. (16) depends on the electron density n as

$$P = \frac{\pi\hbar^2 n^2}{2m_e^*}. \tag{18}$$

Equations (16) and (17) should be solved together with Maxwell's equations for the plasmon EM field to obtain the self-consistent solution. This will be numerically done in Sec. 3.1.2. In this section, in order to provide an intuitive analytical model, we limit our consideration of the plasma oscillations to the linear analysis sufficient to determine conditions necessary for triggering the plasma instability and growth of the amplitude of the plasma wave. In this case, the EM field can be found in the quasi-static approximation by using the Poisson equation for the self-consistent electric potential $\varphi(\mathbf{r},t)$ of the plasma wave

$$\nabla^2_{x,z}(\varphi) = \frac{en}{\varepsilon_0\varepsilon}\delta(z), \tag{19}$$

$$E_x = -\frac{\partial\varphi(x,z=0)}{\partial x}, \tag{20}$$

where ε is the relative permittivity of the surrounding medium.

We linearize Eqs. (16)-(18) with respect to the small fluctuations of the electron density $\delta n(x,t)$ and average velocity $\delta v(x,t)$ assuming that $n = n_0 + \delta n$, $v = v_0 + \delta v$, where n_0 is the equilibrium electron density and v_0 is the constant electron drift velocity due to DC source-drain bias. For one Fourier Harmonic δn, δv, $\varphi \propto e^{-ikx+i\omega t}$ we obtain the system of linear algebraic equations for the charge density $\rho = -e\delta n$ and electric current density $j = -e(n_0\delta v + v_0\delta n)$ in the plasma wave which should be solved together with the Poisson equation connecting ρ and ϕ. Electric potential is connected with the fluctuation of electron density by Eq. (19). When the ideal metal gate is separated by the distance d from the channel, Eq. (19) yields the following relation between φ and ρ [75]:

$$\varphi = \frac{\rho}{|k|\varepsilon\varepsilon_0(1+\coth|k|d)}. \tag{21}$$

A non-trivial solution for j and φ exists only if:

$$\begin{gathered}(\omega - kv_0)\left(\omega - kv_0 - \frac{i}{\tau}\right) = \\ \frac{e^2 n_0|k|}{m_e^*\varepsilon\varepsilon_0(1+\coth|k|d)} + \frac{1}{2}k^2 v_{v_F}^2,\end{gathered} \tag{22}$$

where v_F is the Fermi velocity in the degenerate 2DEG. The last equation is the dispersion equation for the drifting plasmon in the gated 2D electron channel. It can be further simplified if we assume that the collisional damping is small $\omega\tau \gg 1$ and the gate-to-channel separation d is much smaller than the plasmon wavelength $kd \ll 1$. As shown below, the typical plasmon wavelength is of the order of the source-drain distance so the last assumption is justified. With these assumptions, the drifting plasmon dispersion law takes simple form

$$\omega = \left(v_0 \pm v_p\right)k + \frac{i}{2\tau}, \tag{23}$$

where sign $\pm$ corresponds to the Doppler-shifted acoustic plasmons propagating in the opposite directions, and

$$v_p = \sqrt{\frac{e^2 n_0 d}{\varepsilon_0\varepsilon m_e^*} + \frac{v_F^2}{2}} \tag{24}$$

is the plasmon velocity in the absence of the drift. This last result differs from the well-known expression for the velocity of the gated plasmon [75] by the correction $\frac{v_F^2}{2}$. This correction results from the inclusion of the pressure term into the Euler equation.

The general expressions for the voltage $V(x,t) = \varphi(x,z=0,t)$ and the current $I(x,t) = j(x,t)W$ in the plasma wave of frequency ω propagating in the gated channel of width W are

$$V(x,t) = C_1 e^{-ik_+x+i\omega t} + C_2 e^{-ik_-x+i\omega t}, \tag{25}$$

$$\begin{aligned}I(x,t) =& \frac{C_1}{Z_0}\left(1+\frac{v_0}{v_p}\right)e^{-ik_+x+i\omega t} - \\ & \frac{C_2}{Z_0}\left(1-\frac{v_0}{v_p}\right)e^{-ik_-x+i\omega t},\end{aligned} \tag{26}$$

where $k_{\pm} = \frac{\left(\omega - \frac{i}{2\tau}\right)}{\left(v_0 \pm v_p\right)}$ are the complex wave numbers of the plasma wave propagating in the direction of the drift (+) and in the opposite direction (−), and $Z_0 = \frac{d}{\varepsilon\varepsilon_0 v_p W}$. Constants C_1 and C_2 are determined by the boundary conditions.

The Dyakonov-Shur Instability The physical mechanism of the DS instability described in the Introduction is based on the asymmetric reflection of the drifting plasma waves at the opposite ends of the plasmonic cavity formed in the gated region of the 2D conduction channel in the HEMT. The very general description of this reflection can be obtained by introducing the terminating complex impedances between the 2D channel and the gate at the ends of the plasmonic cavity. This approach is based on the analogy between the plasma wave propagation in the gated 2D channel and an ac signal propagation in the transmission line [76].

We assume that an ac link between the 2D channel and the gate is purely reactive and choose the terminating impedances as iZ_S and iZ_D where subscripts "S" and "D" refer to the source and drain sides of the plasmonic cavity and Z_S, Z_D have real values. In this approximation, we neglect the resistive part of the terminating impedances responsible for the leakage of the plasma wave from the cavity to the source and drain contacts with the loss of the real power. Now the boundary conditions for the plasma waves in the plasmonic cavity of length L with terminating impedances iZ_S at $x = 0$ and iZ_D at $x = L$ are:

$$V(0,t) = -iZ_S I(0,t), \tag{27}$$

$$V(L,t) = iZ_D I(L,t), \tag{28}$$

The opposite signs in the right hand sides of these two equations are due to the reversed directions of the currents at the opposite ends of an isolated cavity. Equations (25)-(28) solved together determine the dispersion equation of the plasma modes in the cavity as

$$e^{2\frac{\left(\omega - \frac{i}{2\tau}\right)L}{v_p\left(1-\frac{v_0^2}{v_p^2}\right)}} = \frac{\left[1 - \frac{iZ_D}{Z_0}\left(1 + \frac{v_0}{v_p}\right)\right]\left[1 - \frac{iZ_S}{Z_0}\left(1 - \frac{v_0}{v_p}\right)\right]}{\left[1 + \frac{iZ_D}{Z_0}\left(1 - \frac{v_0}{v_p}\right)\right]\left[1 + \frac{iZ_S}{Z_0}\left(1 + \frac{v_0}{v_p}\right)\right]}. \tag{29}$$

The last equation yields complex plasma frequency $\omega = \omega' + i\omega''$. In the practically important limit $\frac{v_0}{v_p} \ll 1$, we obtain

$$\omega' = \frac{v_p}{L}\left(\pi n - \varphi_S - \varphi_D\right), n = 1, 2, \ldots \tag{30}$$

$$\omega'' = -\left[\frac{v_0}{L}\left(\cos^2\varphi_S - \cos^2\varphi_D\right) - \frac{1}{2\tau}\right], \tag{31}$$

where

$$\tan\varphi_{D,S} = \frac{|Z_{D,S}|}{Z_0}. \tag{32}$$

Inequality $\omega'' < 0$ is the condition of the DS instability in the plasma wave. It follows from Eqs. (30) and (31) that the DS instability occurs only if $|Z_D| > |Z_S|$ at the drift velocities v_0 larger than some threshold value increasing at short relaxation times. One should also point out that the condition $|Z_D| > |Z_S|$ is a necessary condition for the beginning of the DS instability at arbitrary values of $\frac{v_0}{v_p} < 1$ [77]. The magnitude of the instability increment depends on the relative values of $|Z_D|$ and $|Z_S|$ but also strongly depends on the $\frac{|Z_{D,S}|}{Z_0}$ ratio. The impedance Z_0 can be interpreted as the characteristic impedance of the plasmonic transmission line [76]. The proper tuning of the terminating impedances with respect to Z_0 may increase the instability increment. The ideal case corresponding to $Z_S = 0$, $Z_D \to \infty$ was considered in the original paper by Dyakonov and Shur [24]. In this limit, Eqs. (30)-(32) reproduce the results found in this paper at $v_0 \ll v_p$.

3.1.2 Multi-physics Simulation Modeling

The previous analytical solutions were obtained within the first order perturbation theory and, thus, only valid when the fluctuations are small. Less restrictive numerical simulations, which can capture the impact of the geometry, additional plasma damping due to finite electron momentum relaxation time, and the finite values of the terminating impedances, are needed for comprehensive study of the HEMT THz device performance.

The Platform To numerically analyze plasma waves in the on-chip THz source, the hydrodynamic model equations describing the evolution of the electron density n, velocity v and current density $j = -env$ in the 2DEG layer and Maxwell's equations describing the evolution of the electric E and magnetic H fields have to be self-consistently solved together. Since existing commercial tools cannot simultaneously solve both hydrodynamic and Maxwell's equations in the time domain, we have developed a finite-difference time-domain (FDTD) multi-physics simulation platform. In the developed platform, the electron dynamics in the 2DEG layer is described by solving the hydrodynamic model equations Eqs. (16) and (17). To compute E_x in Eq. (16), we now solve Maxwell's equations

$$\nabla \times \boldsymbol{E} = -\mu_0 \frac{\partial \boldsymbol{H}}{\partial t}, \tag{33}$$

$$\nabla \times \boldsymbol{H} = \boldsymbol{J} + \varepsilon\varepsilon_0 \frac{\partial \boldsymbol{E}}{\partial t}. \tag{34}$$

Here $\boldsymbol{E} = E_x\hat{x} + E_y\hat{y}$ and $\boldsymbol{H} = H_z\hat{z}$ refer to the electric and magnetic fields vectors, respectively, the current density vector $\boldsymbol{J} = J_x\hat{x}$ is related to the surface current density j in the 2DEG as $J_x = \frac{j}{t_{2DEG}}$ where t_{2DEG} is the thickness of the 2DEG layer.

Stabilizing a fully explicit discretization of the governing equations for such a highly non-linear system of differential equations as the hydrodynamic model equations is a critical task. A slight change in the discretization strategy may cause computational instability and direct application of common discretization methods does not lead to the physically correct results. The order in how the various quantities (n, v, j, $\boldsymbol{E}$, $\boldsymbol{H}$) are updated is also of crucial importance. In our analysis, we follow the methodology introduced in [78] to simulate the 2DEG as a 1D system and utilize the *up-wind* approach to stabilize the discretization of the system. Then, we use a homogeneous and uniform mesh to generalize to two dimensions for the EM solver [79–81].

In Fig. 17, we illustrate the reference structure simulated in our analysis. It consists of a HEMT-like structure, built with a III-V semiconductor material with permittivity ε and metallic gate and source and drain contacts with conductivity σ. The 2DEG layer is characterized by the electron density n, velocity v, effective electron mass m_e^*, and electron momentum relaxation time τ. It is positioned at a distance d under the gate, and has an effective thickness t_{2DEG}. The impedances between the source and the gate and the drain and the gate are given by Z_S and Z_D, respectively. The HEMT is considered to be in an air-filled box delimited by a Perfectly Matched Layer. The latter is needed to emulate an infinite space when solving Maxwell's equations and prevents artificial reflections at the box boundaries.

Numerical Results In this section, we numerically investigate the behavior of the DS plasma instability in the gated InGaAs-based HEMT structure shown in Fig. 17, with 2DEG channel length $L = 110$ nm, gate length $L_g = 100$ nm extended from source to drain with 5 nm separation from ohmic contacts at source and drain. We consider the gate and source and drain contacts to be made of a nearly ideal metal with $\sigma = 10^7$ S/m, channel depth $d = 70$ nm, channel width W=100 μm, 2DEG layer thickness t_{2DEG}=5 nm, ε=13, $m_e^* = 0.04m_0$. We initialize the whole channel with equilibrium electron density $n_0 = 2.2 \times 10^{15}$ m^{-2} and constant drift velocity v_0, and apply initial excitation by doubling the electron density at the channel length of 5 nm next to the drain contact. Then we record the time dependence of the plasmonic ac current in the 2DEG channel.

Impact of Drift Velocity v_0 and Relaxation Time τ

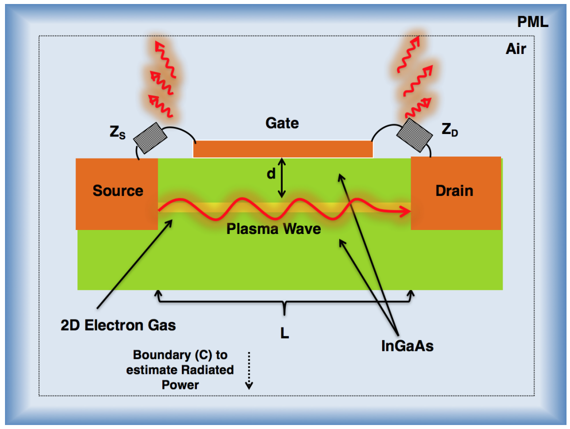

Fig. 17: Schematic of the HEMT structure used for numerical simulations.

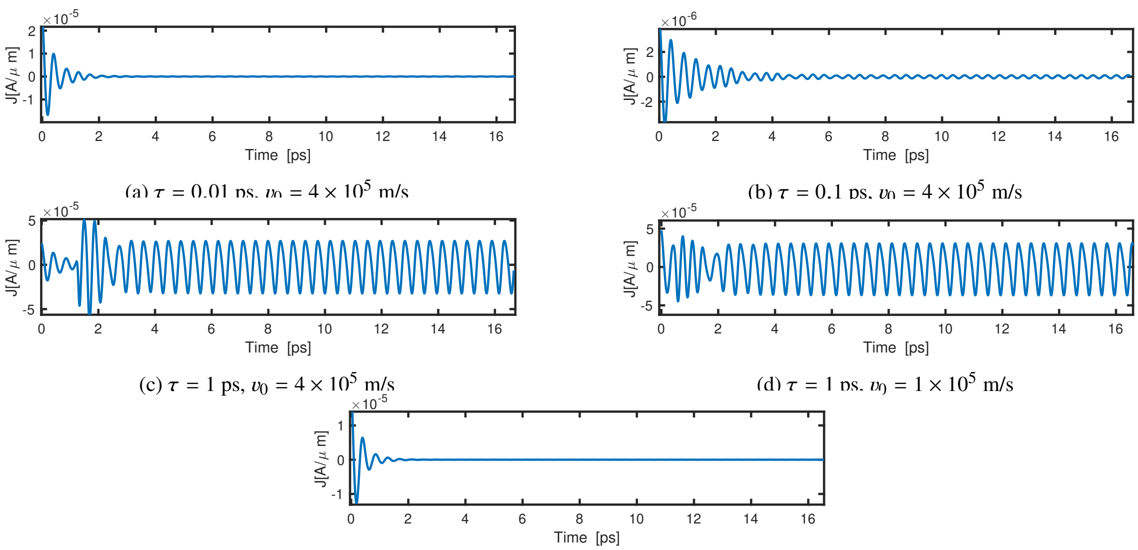

(a) $\tau = 0.01$ ps, $v_0 = 4 \times 10^5$ m/s

(b) $\tau = 0.1$ ps, $v_0 = 4 \times 10^5$ m/s

(c) $\tau = 1$ ps, $v_0 = 4 \times 10^5$ m/s

(d) $\tau = 1$ ps, $v_0 = 1 \times 10^5$ m/s

(e) $\tau = 1$ ps, $v_0 = 0.2 \times 10^5$ m/s

Fig. 18: Plasmonic THz current density j as a function of time at different drift velocities v_0 and electron relaxation times τ. The gate-source impedance $Z_S = 0$, the gate-drain impedance $Z_D = \infty$.

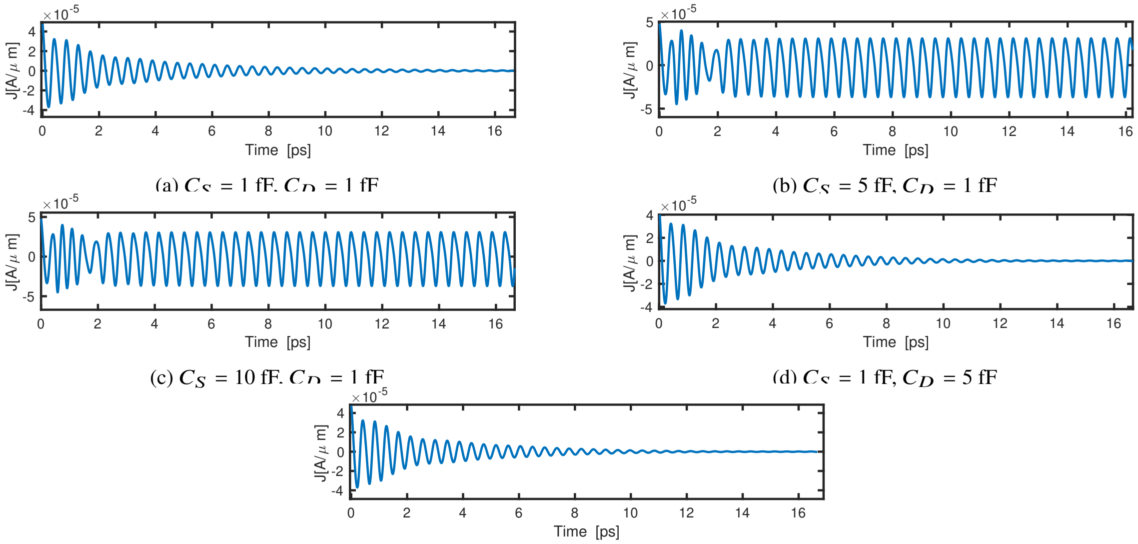

(a) C_S = 1 fF, C_D = 1 fF

(b) C_S = 5 fF, C_D = 1 fF

(c) C_S = 10 fF, C_D = 1 fF

(d) C_S = 1 fF, C_D = 5 fF

(e) C_S = 1 fF, C_D = 10 fF

Fig. 19: Plasmonic THz current density j as a function of time at different values of the gate-source (C_S) and the gate-drain (C_D) capacitances. Electron drift velocity $v_0 = 4 \times 10^5$ m/s, electron relaxation time τ=1 ps

In this numerical study, we assumed the ideal boundary conditions Z_S=0, $Z_D = \infty$ and recorded the time dependence of the plasmonic ac current near the drain contacts after initial excitation. It follows from Eq. (31) that under the ideal boundary conditions the instability occurs when the electron transit time in the HEMT $\tau_{tr} = L/v_0$ is shorter than 2τ [24]. Our numerical results are presented in Fig. 18.

In Figs. 18a through 18c we assumed $v_0 = 4 \times 10^5$ m/s so that the electron transit time τ_{tr}=0.275 ps, and recorded the current signal at different values of the electron relaxation time. For the values of τ=0.01 ps and τ=0.1 ps in Figs. 18a and 18b respectively, we have $\tau_{tr} > 2\tau$, and the plasmonic current signal decays rapidly after the initial excitation because the power losses due to random electron scattering exceed the power gain due to plasmon reflections from the asymmetric boundaries. In Fig. 18c, the value of τ is 1ps and $\tau_{tr} < 2\tau$. In this case, the power gain at the plasmon reflections from the asymmetric boundaries starts to exceed the scattering losses, and the DS instability develops. The oscillating THz plasmonic current stabilizes at some finite amplitude when the combined losses due to scattering and EM radiation balance the power gain.

Decreasing electron drift velocity makes electron transit time longer and the instability eventually disappears. This is shown in Figs. 18d and 18e where we recorded the time dependence of the current at τ=1 ps but $v_0 = 1 \times 10^5$ m/s and $v_0 = 0.2 \times 10^5$ m/s, respectively. In Fig. 18d the value of τ_{tr}=1.1 ps is less than 2τ and the instability still exists. However, with further decrease of v_0 the DS instability disappears as shown in Fig. 18e where τ_{tr}=5.5 ps.

Impact of Source and Drain Impedances

In the HEMT plasmonic cavity formed in the 2D channel between the source and the drain terminal, the DS instability is maximized under the ideal boundary conditions $Z_S = 0$, $Z_D = \infty$. As shown in Eq. (31), the finite source-gate and drain-gate impedances suppress the instability. These impedances are the result of the shunt capacitances always present between the gate and the HEMT source/drain terminals. Calculations show that in the HEMT structures these impedances are in the range of tens of femtofarads [25]. We studied numerically the impact of the finite gate-source (C_S) and gate-drain (C_D) capacitances on the DS instability in the HEMT structure shown in Fig. 17. In this case, the boundary conditions conforming with Eqs. (27)

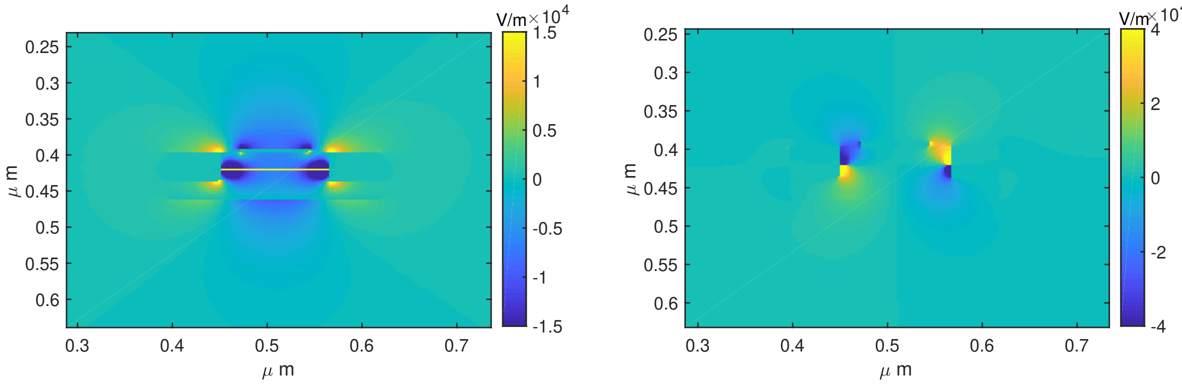

(a) E_x (b) E_y

Fig. 20: Electric fields resulting from the DS instability corresponding to Fig. 18c (ideal boundary conditions, τ = 1 ps, $v_0 = 4 \times 10^5$ m/s).

and (28) are as follows

$$I(0,t) = -C_S \frac{\partial V(0,t)}{\partial t}, \tag{35}$$

$$I(L,t) = C_D \frac{\partial V(L,t)}{\partial t}, \tag{36}$$

where $V(x,t)$ is connected to $n(x,t)$ as $V(x,t) = -en(x,t)/C_{gc}$. Here $C_{gc} = \varepsilon\varepsilon_0/d$ is the gate-channel capacitance per unit area.

In our numerical simulations, we take $v_0 = 4 \times 10^5$ m/s and τ=1 ps and record plasmonic current near the drain contact as a function of time. The results are presented in Fig. 19.

In Fig. 19a, we assumed that $C_S = C_D$=1 fF. In this case, the boundaries become symmetric ($Z_S = Z_D$), the power gain disappears, and the ac plasmonic current rapidly decays due to random scattering of electrons. In Figs. 19b and 19c, asymmetry is introduced by assuming that C_S =5 fF and 10 fF, respectively, and C_D=1 fF so that $Z_D > Z_S$. The power gain due to plasmon reflections from the asymmetric boundaries exceeds the damping losses, and the DS instability develops with finite plasmonic current stabilized by the radiation losses. If the value of C_S is kept constant, and asymmetry is introduced by increasing the value of C_D so that $Z_D < Z_S$ the current continues to decay as predicted by Eq. (31). This is shown in Figs. 19d and 19e where C_S=1 fF and C_D=5 fF and 10 fF, respectively.

Rigorous numerical solution of the non-linear hydrodynamic equations together with the full system of Maxwell's equations is in good qualitative agreement with the results of the linear perturbation analysis of the hydrodynamic equations within quasi-static model of the EM field presented before. However, the full numerical solution goes beyond the linear response and allows analysis of the final steady state of the radiating HEMT system including the structure of the radiated THz EM field. This analysis is presented in the next section.

Generated Electromagnetic Fields In this section, we examine the performance of a HEMT-like structure as a THz EM source based on the DS instability by analyzing the properties of the generated fields and the impact of the source and drain impedances on the radiated power.

In Figs. 20a and 20b, the electric field vector components E_x and E_y respectively, are plotted for the radiating HEMT in the steady state with τ=1ps, $v_0 = 4{\times}10^5$ m/s and ideal boundary conditions corresponding to Fig. 18c. The plots show that the plasma wave in the 2DEG channel generates an EM wave in the space between the gate and 2DEG channel, which leaks through the gaps between the source/drain contacts and the gate and propagates eventually over the entire simulation region.

The EM power P radiated by the THz source at any given frequency can be calculated by integrating the

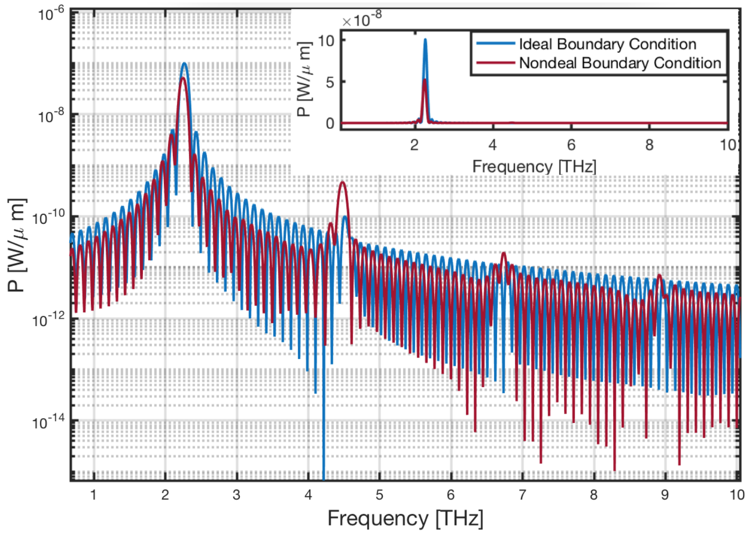

Fig. 21: The radiated EM power spectrum for ideal boundary conditions (blue) and non-ideal boundary conditions (C_S = 10 fF, C_D = 1 fF) (red), τ=1 ps, $\upsilon_0 = 4 \times 10^5$ m/s. Inset: the same power spectrum in linear scale, showing the power loss due to non-ideal boundary conditions.

normal component of the Pointing vector over a continuous boundary that encircles the device as:

$$P = \frac{1}{2} \int_C Re \left\{ \widetilde{\boldsymbol{E}} \times \widetilde{\boldsymbol{H}}^* \right\} \boldsymbol{n} dl, \tag{37}$$

where $\boldsymbol{n}$ is the unit vector normal to the boundary and $\widetilde{\boldsymbol{E}}$ and $\widetilde{\boldsymbol{H}}$ are complex Fourier transforms of the electric and magnetic field vectors in the time domain at the integration boundary C shown in Fig. 17. In our analysis, we disregard the transient time until the generated currents and fields become stable (approximately the first 2 ps in Figs. 18 and 19).

In Fig. 21, we show the radiated EM power spectrum for both ideal and non-ideal (C_S = 10 fF, C_D = 1 fF) boundary conditions at τ=1 ps and $\upsilon_0 = 4 \times 10^5$ m/s. Resonant peaks in the power spectrum occur at the frequencies of plasmons confined in the HEMT cavity with the largest peak at the fundamental frequency of 2.27 THz and much weaker peaks at higher harmonics. The value of the fundamental plasma frequency estimated from the power spectrum is about 10% larger than the one predicted by the theoretical model in Eq. (29) indicating the difference between simple theoretical model and more accurate numerical simulation accounting for complicated spatial distribution of the EM fields in the finite structure, see Fig. 20.

At the fundamental frequency, the radiated EM power per unit channel width shown in Fig. 21 is about 9×10^{-8} W/μm under the ideal boundary conditions. In this case, the total radiated power from the device can be estimated as 9×10^{-8} W/μm ×100μm= 9μW. The non-ideal boundary conditions decrease the instability increment in Eq. (31) and result in the decreased radiated EM power. This is shown in the inset in Fig. 21 where the radiated power spectrum is plotted in the linear scale making this difference more clear. When the non-ideal boundary conditions are used the reduction in the radiated power at the fundamental frequency is about 4.2×10^{-8} W/μm or 46.7%.

3.1.3 Device Fabrication and Experimental Characterization

In this component of the project, we are working towards the fabrication and experimental characterization of the flexible, on-chip THz source that functions via the resonant excitation of two-dimensional plasmons in compound-semiconductor FETs. As discussed in the previous section, an important requirement for the observation of this instability is that the plasmon reflection conditions at opposite ends of the channel (the drain and source boundaries) must be very different to one another (i.e. they should be strong asymmetric).

With such asymmetry achieved, an instability is expected to develop within the channel, causing the amplitude of the induced plasma wave to increase exponentially over time (provided that the plasma-wave gain exceeds damping losses). In our previous report, we described how we proposed to realize this condition in InGaAs FETs in the which the required asymmetry is implemented by including a narrow, sub-micron, constriction at one end of the transistor channel.

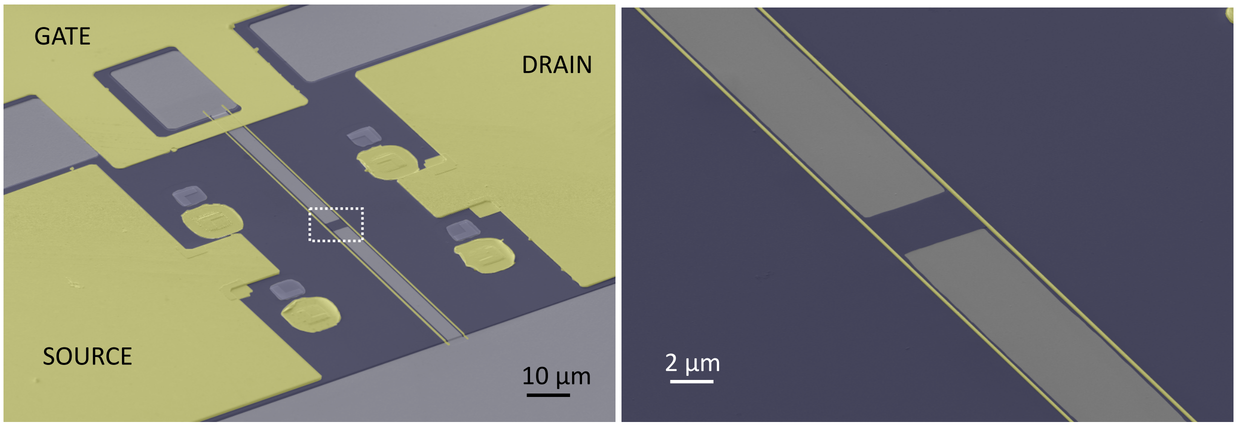

Fig. 22: Fabricated InGaAs/InAlAs FET with plasmonic cavity and asymmetric source/drain conditions. The figure on the left is a global view of the device, showing source, drain and gate contacts. The figure on the right is an expanded view of the section enclosed by the white dotted line on the left. This expanded view shows the narrow (200-nm wide) metal gates that define the plasmon cavity on either side of the constriction (the two lighter, rectangular regions correspond to etched regions of the heterostructure).

In the past twelve months, we have made considerable progress towards the realization of the proposed source. In a collaboration with colleagues at AIST (Tsukuba, Japan), we have designed, fabricated and characterized a tailored InGaAs heterostructure for use as the channel of the FETs. This system consists of a 2DEG that possesses all of the characteristics required for implementation of the plasmonic instability: high electron mobility (80,000 cm^2/Vs at 77 K, 12,000 cm^2/Vs at room temperature), and correspondingly long mean-free path (2 μm and 0.5 μm, respectively); high electron sheet density ($>10^{12}$ cm^{-2}), and; a shallow (<30 nm) 2DEG layer that should allow efficient emission of the plasmon-induced radiation. We have also successfully developed a reproducible scheme for the fabrication of the devices, key requirements of which are the ability to cleanly etch the drain constriction and to carefully align a narrow metal gate relative to the edge of this constriction. The gate itself defines a plasmon cavity that is no more than a couple of hundred nanometers long and which extends over the full width (>100 μm) of the semiconductor mesa. Images of a completed device are presented in Fig. 22, which consists of views of the device at different scales.

The electrical properties of the fabricated FETs have been measured over a wide temperature range (3–300 K) in order to provide evidence for the expected plasmon instability. At this stage, our focus has been on providing such evidence in studies of the DC electrical characteristics of the devices. Theoretically, the onset of the DS instability is expected to be manifested in the I_d-V_d characteristics of the devices, presenting as a sudden drop in the channel current when the drain bias is increased beyond the value required to support the instability. We systematically observe evidence of such an effect in our devices, as we demonstrate in Fig. 23.

In the left panel of Fig. 23 we show the influence of varying the gate voltage on the measured I_d-V_d characteristics of one of our devices. These curves each feature an instability (denoted by the arrows), according to which the current exhibits a sudden drop when the drain bias is increased beyond a certain value. As the gate voltage is made more negative the visibility of this feature is suppressed, a trend that presumably reflects the suppression of the plasmonic instability when the carrier concentration is lowered below some characteristic value by the gate. In the right panel of Fig. 23, we demonstrate the temperature dependence of this feature and show that it survives as we approach liquid-nitrogen temperature. This is quite understandable, since our analysis of the 2DEG Hall mobility (not presented here) demonstrates that

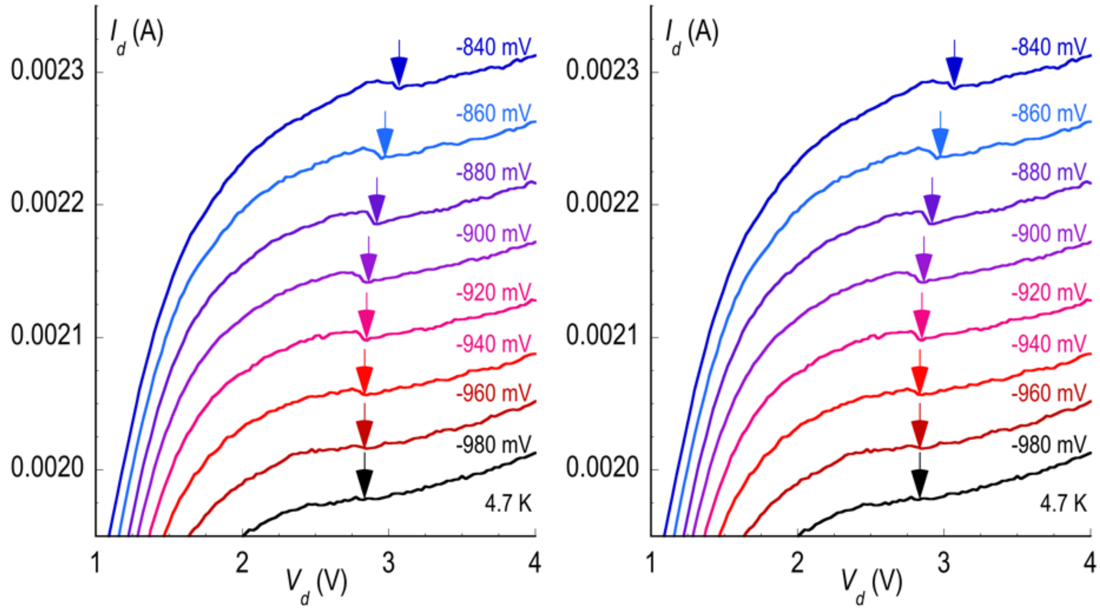

Fig. 23: Electrical characteristics of a fabricated InGaAs/InAlAs FET with plasmonic cavity and asymmetric source/drain conditions. The figure on the left shows the I_d-V_d characteristics obtained with various voltages (indicated) applied to the gate of the device. Arrows denote the presence of a current instability that shifts systematically with variation of the gate voltage. The right panel shows the temperature dependence of the instability, demonstrating its survival to temperatures approaching those of liquid nitrogen.

the mean-free path for electrons remains relatively unchanged over this temperature range. The ballistic-transport conditions required for the DS instability should therefore be preserved over this range, allowing us to observe this feature.

As noted already, an important requirement for the DS instability is the presence of asymmetric source and drain coupling to the channel. More specifically, the coupling to the drain should be much weaker than that to the source and this is achieved in our experiment by the introduction of the etched constriction. If the role of the source and drain contacts is reversed in our devices, we therefore expect that the current instability associated with the DS instability should not be observed. Although not shown here, this is indeed what we observe in our experiments, providing further confidence that the results presented here are indeed related to the DS instability.

Based on the progress made in the current reporting period, our objective in the coming year is to search for evidence of the THz emission that should be associated with the DS instability. To this end, we plan to collaborate with Prof. Peter Liu within our department, using his high sensitivity THz bolometer system to detect this radiation. We are already collaborating with Prof. Liu (see below) in this area, and will initiate our detection studies in the coming weeks. The experimental effort will be supported by the modeling program described above, which should allow us to clarify the conditions required for observation of the desired instability.

3.2 Graphene-based Plasmonic Nano-antenna Arrays

3.2.1 Hybrid Graphene/Metal Reflecting Antenna: Analytical and Numerical Modeling

As we presented in [42], and summarized in the first year project report, the performance of an antenna array is determined both by the design of each individual radiating element as well as by the mutual coupling between neighboring elements. As important as the array geometry, the way in which the radiating elements are fed controls the number, direction and width of the resulting beam(s). While the development of the on-chip THz sources will allow the integration of a THz source per antenna, for the time being and in order to be able to test the performance of the antennas by means of the THz spectroscopy tools available to the team, we are interested in the design of neither transmit- nor receive- but reflect-arrays.

The theory of reflect-arrays works on a similar principle to transmit and receive arrays, with the key difference being that the each element in the reflect-array is excited by an incoming wave instead of a port, and there is no transmission line. As in our previous designs (described in last year report), our fundamental element is a patch antenna. The strength of the reflected field from a graphene-based patch antenna depends very strongly on the conductivity of the graphene patch, which on its turn largely depends on the scattering time τ for electrons in the graphene layer. In our original analysis, we considered values of τ in the order of hundreds of femtoseconds, as common practice in the related literature. However, in light of the experimental characterization results described in Sec. 2.2.2, the scattering time for the structures that we are able to fabricate is much lower, in the order of tens of femtoseconds at most.

In Fig. 24, we illustrate the reflected field from a graphene-based plasmonic nano-antenna for two different values of the scattering time, namely, 500 fs (left) and 31.5 fs (right). For the large scattering time, a clear resonant structure can be seen, resulting from the SPP wave successfully traveling end-to-end in the cavity. However, for low scattering time, the SPP wave dies before reaching the end of the cavity, preventing the resonance to arise. As a result, the reflected (and, similarly, radiated) field is much lower.

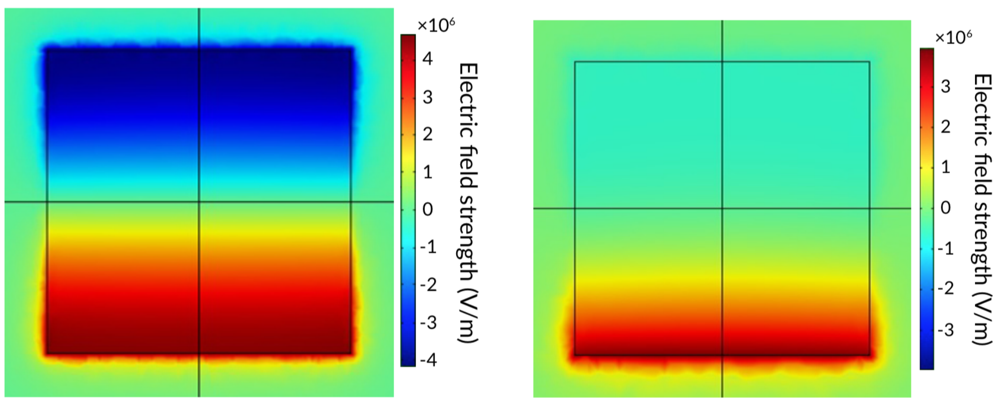

(a) τ=500 fs (b) τ=31.5 fs

Fig. 24: Reflected field from a graphene-based plasmonic nano-antenna for two different values of the scattering time in graphene.

In order to overcome this limitation, one option consists in creating a hybrid structure, in which a metal is utilized as the reflecting element, and graphene is utilized as the tuning element, for example, to control the phase of the antenna reflection coefficient. In this case, the design of the reflecting element or antenna is straight forward and obeys the classical theory for metallic antennas. As an example, in Fig. 26, we illustrate a resonant reflecting patch antenna designed to operate at 1.5 THz (the center frequency of our THz spectroscopy platform), with length L=63.2 μm and width W=49.94 μm, on a 300 nm thick substrate with $\varepsilon = 4$. The much larger dimensions of the antenna are the result of this not being a plasmonic structure, but a regular metallic antenna.

When a layer of graphene is introduced atop the substrate, surrounding the patch, it affects the strength of the electric fields generated on the patch, and subsequently, the strength of the radiated field. As the Fermi energy of the graphene layer is increased, the conductance of the graphene sheet increases, causing electric fields to leak from the patch element. The electric fields generated on the reflect-array patch for two different Fermi levels, 0.1 eV and 0.9 eV are shown in Fig. 25. As expected, the electric fields are significantly weaker in the case of 0.9 eV.

The single element can be replaced by an array of patches. The basic design criteria remains the same as for transmit/receive nano-antenna arrays and was already presented in our previous works. We will experimentally characterize the structures next.

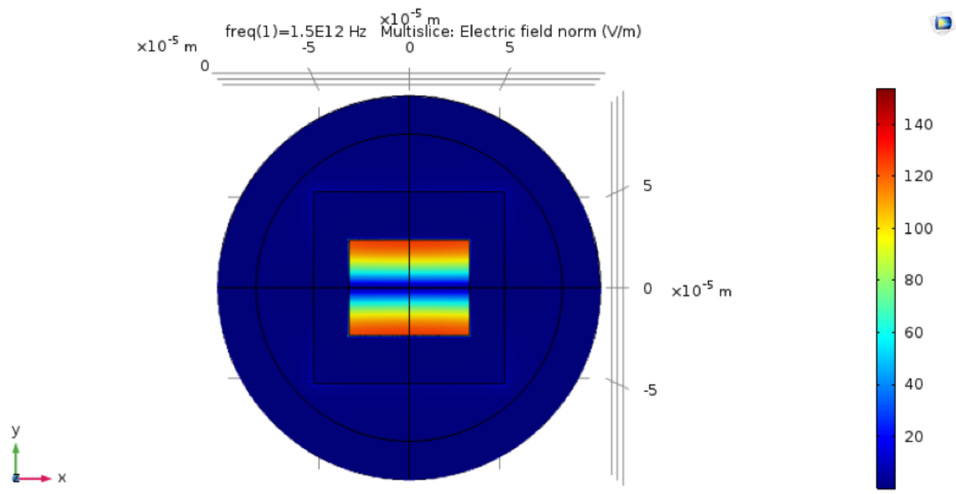

Fig. 25: A metallic patch antenna designed to resonate at 1.5 THz.

3.2.2 Fabrication and Experimental Characterization in Reflection

Although we demonstrated in Year 1 our ability to fabricate various antenna structures made entirely of graphene, the unexpectedly short momentum relaxation time of plasmons in graphene damps the SPP so much that it cannot resonate inside the antenna. Given this information, there are a couple ways to proceed. One is to change or modify the substrate such that scattering is mitigated, and the other is to reconsider the role of graphene in the desired application. We chose the latter, because incorporation of graphene into a hybrid structure will allow us to take advantage of its unique linear bandstructure. Hence we began working on graphene/metal hybrid reflectarrays.

Our first design was based on a metal dipole atop a continuous graphene sheet, as shown in Fig. 27. The operating principle is as follows. The two halves of the structure are quarter-wavelength monopoles, but they are separated by a small (sub-micron) gap. This gap is sufficiently small that it is invisible to a THz wave, yet sufficiently large that the two halves would be electrically isolated. The underlying graphene sheet electrically connects the two halves of the dipole, but the conductivity of this graphene link ultimately depends on the graphene's Fermi energy. Since this can be changed by electrostatic gating, the coupling between the two dipole halves can be modulated by gating the graphene.

The main problem with this approach is that if the structure shown in Fig. 27 is fabricated on a doped Si wafer, to facilitate electrostatic gating of the graphene, the doped wafer itself functions as a ground plane. Since a dipole antenna does not need a ground plane, and ideally should be far from other conductors, this approach contains two competing factors that are impossible to circumvent. A different approach was clearly necessary.

Our second design was one that *requires* a ground plane for efficient radiation. We decided to replace the dipole with a patch antenna, as shown in Fig. 28a In this approach, the doped substrate functions as a ground plane, which forms the cavity by which a patch antenna radiates. Moreover, the Fermi level in the graphene can be modulated by electrostatic gating via the doped substrate. Changing graphene's Fermi level changes its electrical conductivity. Increasing the electrical conductivity softens the electrical boundary condition at the antenna border, weakening the resonance. Hence, increasing (decreasing) the Fermi energy of the underlying graphene should weaken (strengthen) the patch antenna resonance.

We characterized response of array for parallel and perpendicular polarization (Fig. 29a), as well as the response with and without underlying graphene (Fig. 29b). Graphene reduces reflection by softening conduction boundary condition at each element.

In the next funding period, we are going to refine our analytical and numerical designs based on the

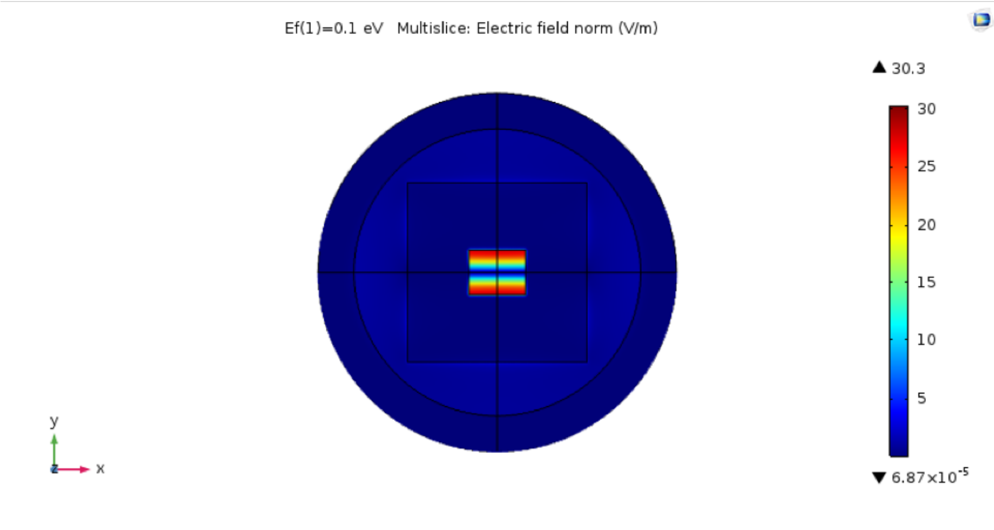

(a) E_F=0.1 eV.

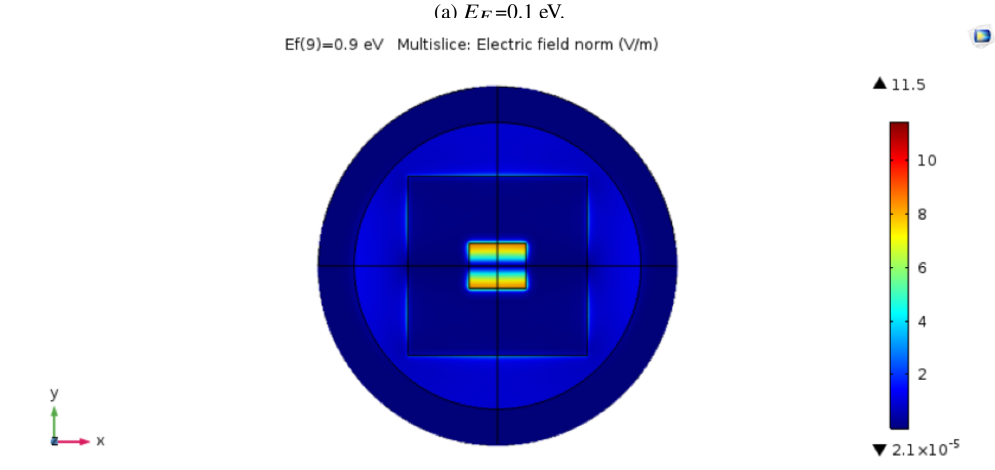

(b) E_F=0.9 eV.

Fig. 26: Impact of graphene Femi energy on the reflected field off a metallic antenna.

extracted parameters, and work toward refining the patterning process. In parallel to the array optimization, we will work toward electrically changing the graphene Fermi energy. This should allow us to moduleate the strength of the reflection.

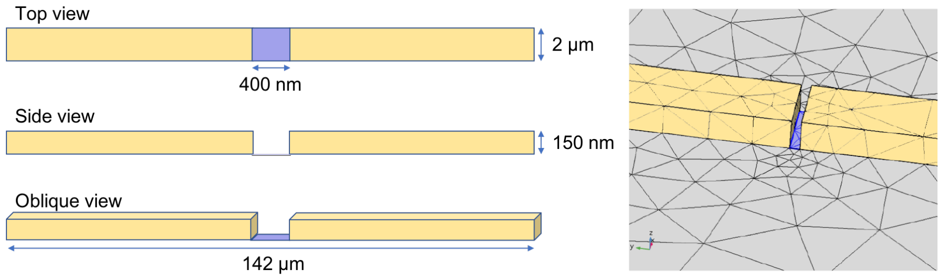

Fig. 27: Schematic of a metal dipole antenna structure atop graphene.

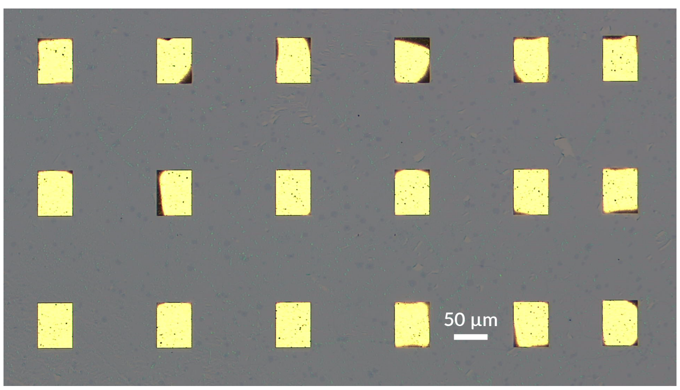

(a) Fabricated metal patches atop monolayer graphene

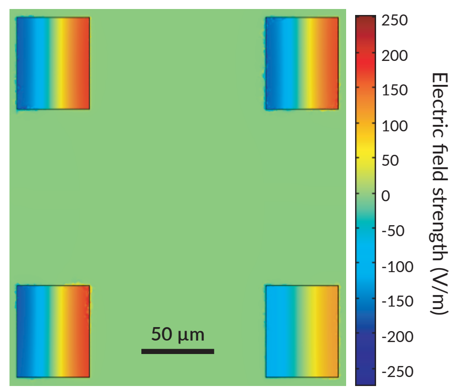

(b) Simulation of array response

Fig. 28: Graphene/metal hybrid patch reflect array fabrication and simulation.

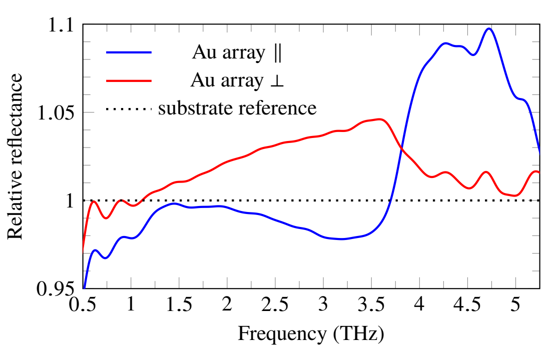

(a) THz reflectance spectra of the Au array relative to the underlying substrate. Reflectance increases at 4.5 THz ($3\lambda/2$ resonance) for parallel but not perpendicularly polarized light.

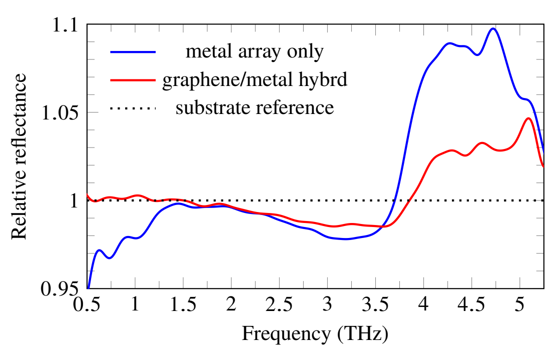

(b) THz reflectance spectra relative to the underlying substrate. Increased reflectance by the array at 4.5 THz is weakened by the presence of graphene.

Fig. 29: THz spectra showing response of metal-only array and the influence of graphene.

4 Year 3

4.1 Hybrid Graphene/semiconductor Plasmonic On-chip Terahertz Source

4.1.1 The Dyakonov-Shur Instability in Graphene-only Nanostructures

In Year 3, the theoretical studies have been focused on analyzing the behavior of the DS instability in graphene nanostructures (Fig. 30. The hydrodynamic Euler equation for the two-dimensional electron fluid in graphene was derived directly as the second moment of the Boltzmann equation for the massless Dirac fermions. At this stage, we included the elastic scattering of electrons on Coulomb impurities into our formalism. This scattering channel dominates in the doped graphene layers at low temperatures. The Euler equation and the equation of continuity subject to the DS boundary conditions have been solved numerically together with the full system of the Maxwell equations, by following a similar approach as that described in Year 2.

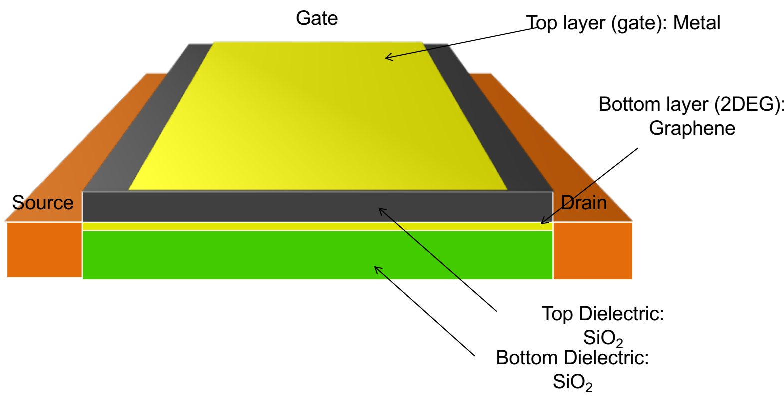

Fig. 30: Schematic of the graphene nanostructure under analysis.

The developed numerical platform allowed us to analyze the DS instability of the plasma oscillations in the gated graphene nanostructures and the THz electromagnetic radiation generated when the plasmons are finally stabilized due to nonlinear processes described by the convection term in the Euler equation. We found conditions necessary for the onset of the instability as a function of the electron scattering time, size of the sample and the DC bias current. The spatial distribution of the radiated THz electromagnetic field and the radiated power have also been found.

In Fig. 31, we provide preliminary results demonstrating the excitation of a THz resonant mode in the graphene nano-structures, in the time and frequency domains and for two different lengths.

We also considered the modulation of the radiated electromagnetic wave using the low frequency modulation of the DC bias current and/or the gate voltage in the graphene transistor. In Fig. 32, we illustrate how the two modulations technique effectively modulate the resulting THz wave. This opens the door to practical THz data modulations, as we illustrate in Fig. 33, where the preservation of the phase between the modulating signal and the THz signal is shown, in the particular case of a Quadrature Phase Shift Keying (QPSK) modulation.

4.1.2 Device Fabrication and Experimental Characterization

In the latest phase of this program, we have undertaken detailed investigations of the electrical characteristics of InGaAs FETs with deliberately-engineered asymmetric boundary conditions. This work built upon our prior studies of negative differential conductance in these structures, to demonstrate a number of quantitative features consistent with the expected nature of the Dyakonov-Shur (DS) plasmonic instability. Our progress on this problem is described below.

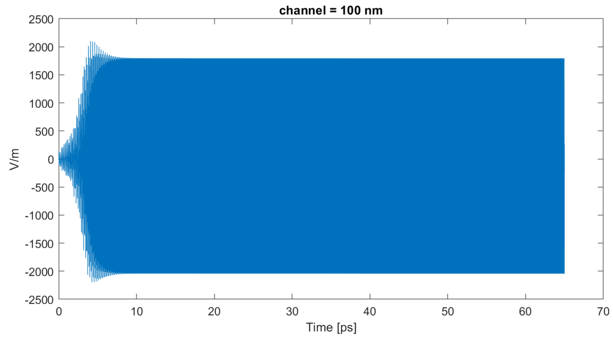

(a) 100-nm-long channel: time domain signal.

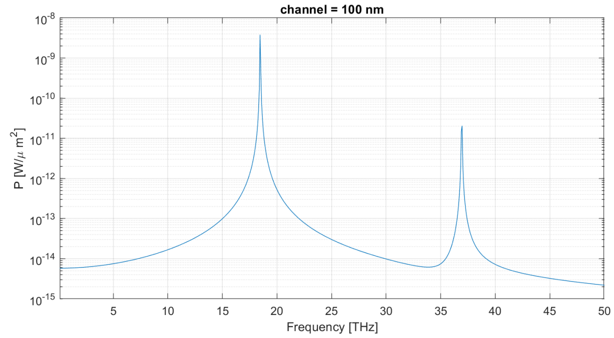

(b) 00-nm-long channel: spectrum.

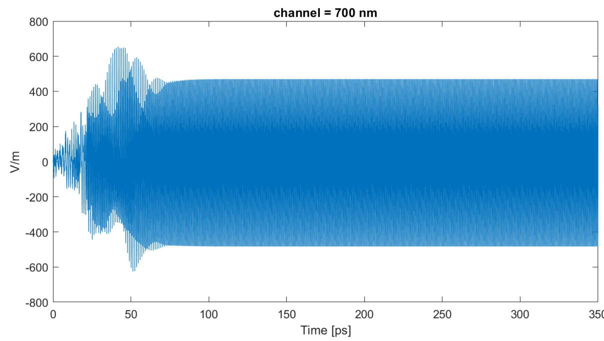

(c) 700-nm-long channel: time domain signal.

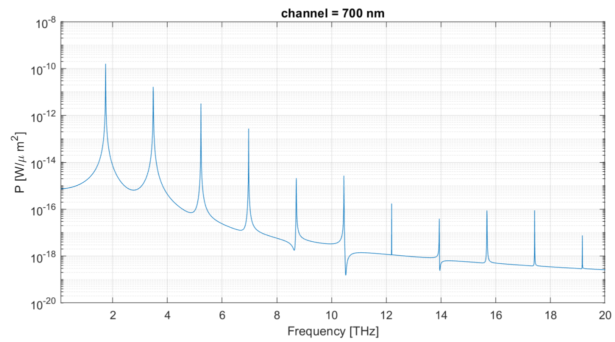

(d) 700-nm-long channel: spectrum.

Fig. 31: Demonstration of the DS instability in graphene nanostructures.

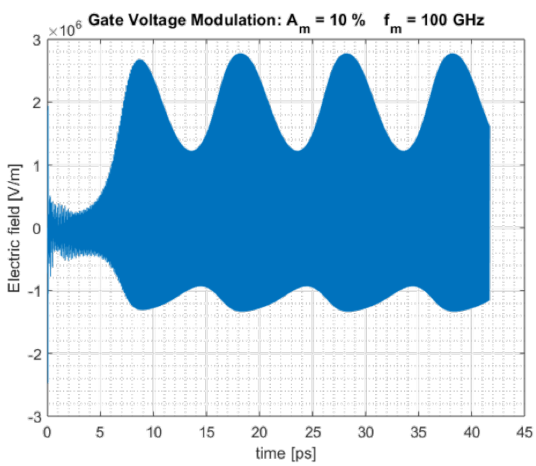

(a) Gate voltage modulation.

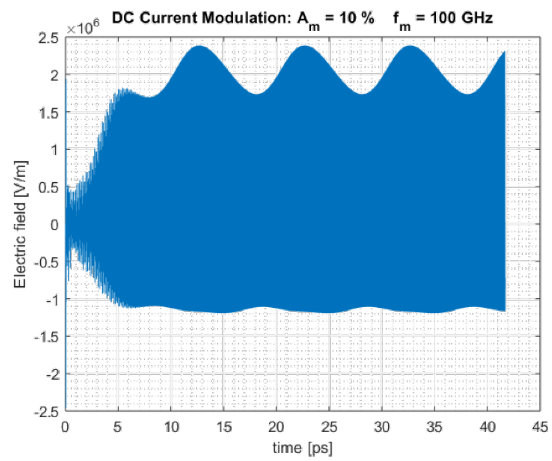

(b) DC bias current modulation.

Fig. 32: Modulation of the DS instability in graphene nanostructures.

Optimization of the asymmetric FET geometry In our earlier work, we had fabricated FET structures in which the plasmonic cavity was connected to source and drain contacts through large reservoirs (10–100 μm), resulting in a significant access resistance to the device. In order to minimize the effect of this resistance, we have fabricated a new generation of devices in which the access length to the plasmonic cavity is reduced to just a few microns. An example of such a device is shown in the inset to Fig. 34, in which we see the ~100 nm metal gate that defines the plasmonic cavity, the constriction needed to ensure current flow from source to drain, and the contact metallization of these two reservoirs. The distance from the source to the gate is just 2 μm, and in the main panel of the figure we show the resulting I-V characteristic. Clear negative differential conductance (NDC) is apparent in these measurements, and is significantly enhanced

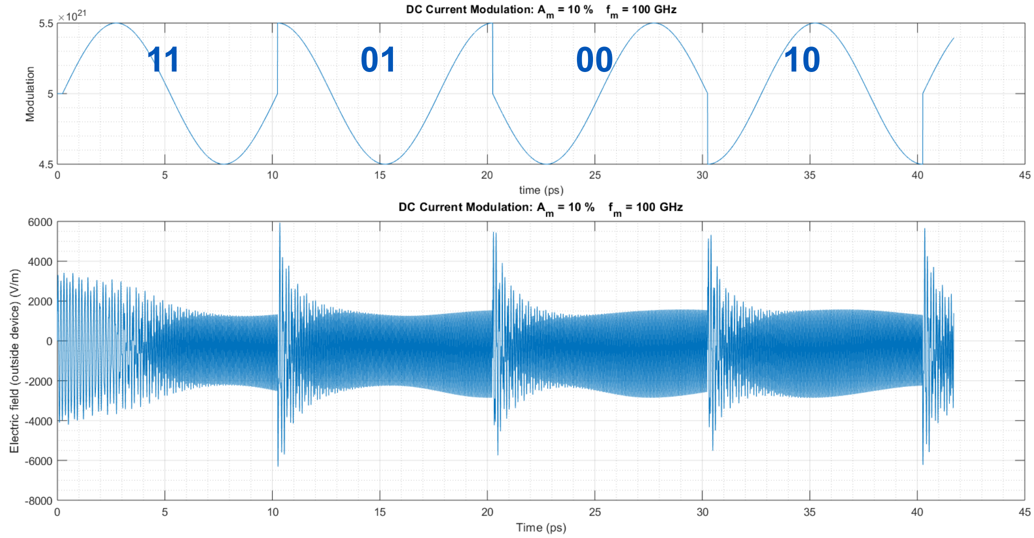

Fig. 33: QPSK data modulation of the DS instability in graphene nanostructures.

over our prior work, in which the size of the NDC was around just 1% of the total current. Here the effect is enhanced by at least an order of magnitude, representing a positive improvement for the prospect of observing THz emission due to the DS effect.

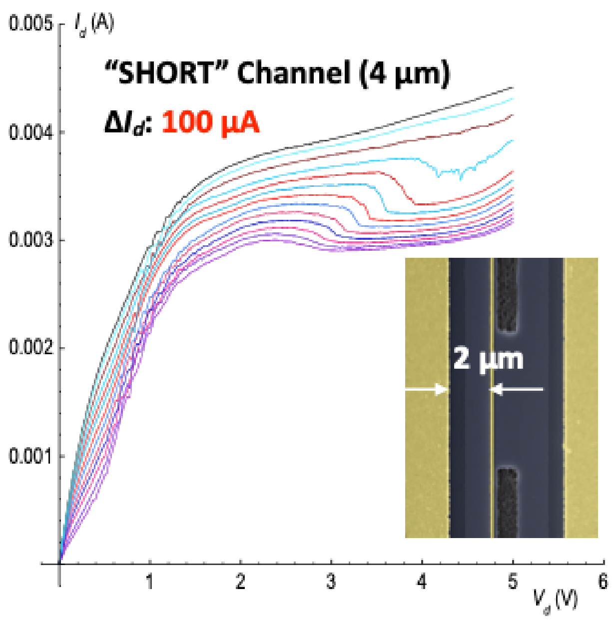

Fig. 34: Transistor curves at different gate voltages, measured at 4.2 K for the InGaAs FET shown in the inset. The NDC that appears for drain voltages in the range of 3-5 V is presumed to arise from the DS instability.

Evidence of Thresholding Behavior in the NDC According to theory, the DS instability, involving plasmonic excitation and emission of THz radiation, is expected to occur once the growth in the plasmonic wave amplitude while transitioning under the FET gate exceeds corresponding damping arising from scattering. This in turn implies that emission onsets once the drift velocity exceeds $L/2\tau$, where L is the length of the plasmonic cavity defined by the gate and τ is the scattering time. To test for evidence of such a thresholding behavior, we have studied the onset of the NDC in the transistor curves and the manner in which this evolves as the gate voltage is used to vary the carrier concentration under the gate. More specifically, the carrier concentration may crudely be taken to be proportional to $(V_g\check{}V_{Th})$, where V_{Th} is the threshold gate voltage of the transistor. Denoting the value of the drain current at which the NDC onsets as IdON (see Fig. 35), the quantity $I_d^{ON}/(V_g\check{}V_{Th})$ should be proportional to the drift velocity at the onset of NDC. In the main panel of Fig. 35, we plot the variation of $I_d^{ON}/(V_g\check{}V_{Th})$ as a function of gate voltage and see that this quantity is essentially constant. This thresholding behavior is consistent with the notion that the NDC observed in experiment is consistent with the DS instability.

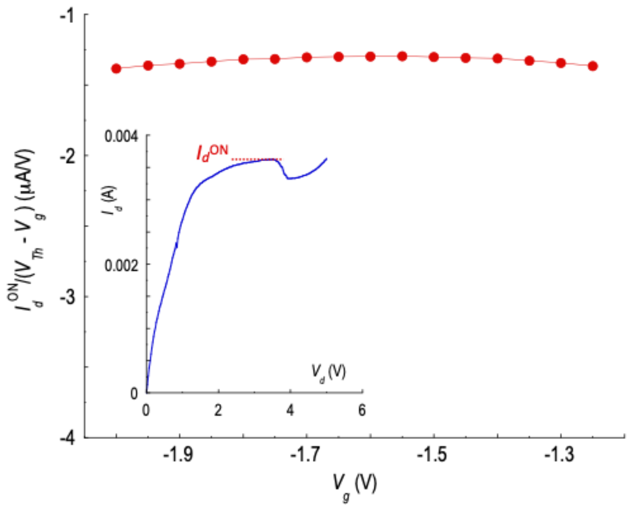

Fig. 35: Evidence of thresholding behavior in the NDC exhibited by our InGaAs FETs. The invariance of the quantity plotted on the vertical axis suggests that NDC onsets whenever the drift velocity reaches a critical value. The inset defines the value of the current at the onset of NDC.

Other Observations The interpretation of the observed NDC in terms of the DS mechanism is bolstered further by several other observations:

- The NDC is only observed for positive, but not negative, drain bias, reflecting the engineered asymmetry in the device structure.
- The NDC is not observed in devices fabricated with the plasmonic gate, but no constriction, a feature that confirms the need for engineered asymmetry in the boundary conditions of the system.
- The NDC is not in devices fabricated without the plasmonic gate, even if a constriction is present, highlighting the need for a plasmonic cavity to realize this phenomenon.
- In the present devices, the NDC persists up to temperatures of around 100 K. This is consistent with the known temperature dependence of the mean-free path in these heterostructures; with increase of the temperature from 4.2 to 100 K, this length scale decreases from more than a micron to around 100 nm.

Ongoing Work While the current funding has expired, we continue to work on this technology and are currently focused on trying to observe the emission of THz radiation from the fabricated devices. Initial attempts at this were made using a THz time-domain spectroscopy system in the Department; this approach was not successful, primarily due to issues with detector sensitivity. At present, we are therefore exploring a different approach in which we will evaluate emission using p-type Ge detectors, mounted in close proximity (~1 mm) to the InGaAs chip.

4.2 Graphene-based Plasmonic Nano-antenna Arrays

In Year 3, we focus on the formal design and operation of hybrid graphene-metal reflect-arrays.

4.2.1 Hybrid Graphene-Metal Reflect-array Design, Modeling and Control

Here, we describe the design of the hybrid reflecting element and its assembly in large arrays. Our system is designed to operate at 1.5 THz (*true* THz frequencies), as this is the center frequency of our experimental setup. The same methodology can be utilized to design the system across the THz band. The resultant free-space wavelength λ_0 is then 199.8 µm.

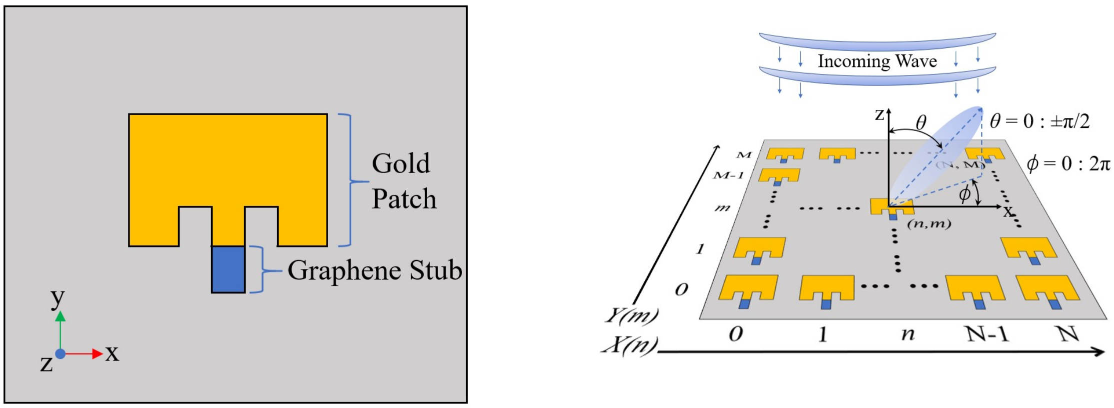

(a) Gate voltage modulation.

(b) DC bias current modulation.

Fig. 36: The design of the hybrid element and the resulting reflectarray.

Single Element Design and Principle

1. Patch: The metallic patch works as a broadside emitter on the basis of radiating slots. For optimal design efficiency at the desired frequency, the thickness of the substrate needs to be in the range of 0.003 – 0.05 λ_0, as given by [69].

The reflection coefficient, or the S11 parameter, is the accepted performance metric for a patch antenna. The lower the S11 in transmission, the higher the efficiency [69]. By the reciprocity principle, a good transmitting patch is also a good receiver. Since a reflectarray element is required to be a good receiver as well as a good transmitter, the patch so designed is a resonant reflectarray element [82].

The dimensions of the patch are modelled from the cavity model equations (38), (39) and (40), as per [69]:

$$W = \frac{c}{2f_0\sqrt{\frac{\varepsilon_r+1}{2}}}, \tag{38}$$

$$\varepsilon_{\text{eff}} = \frac{\varepsilon_r + 1}{2} + \frac{\varepsilon_r - 1}{2}[1 + 12h/W]^{-1/2}, \tag{39}$$

$$L = \frac{c}{2f_0\sqrt{\varepsilon_{\text{eff}}}} - 0.824h\left[\frac{(\varepsilon_{\text{eff}} + 0.3)(\frac{W}{h} + 0.264)}{(\varepsilon_{\text{eff}} - 0.258)(\frac{W}{h} + 0.8)}\right]. \tag{40}$$

Here, W and L are the width and the length of the patch antenna at a desired frequency of f_0 and h is the thickness of the substrate. ε_r represents the dielectric constant of the substrate, while ε_{eff} represents the effective dielectric constant, since the electric fields of the patch antenna undergo fringing at the boundary of the substrate.

2. Stub: We implement phase control through a graphene based stub, which acts as a waveguide with an active graphene layer [37]. The properties of the SPP waves generated in this waveguide are captured by the complex wave vector k_{spp}. More specifically, as shown in (41) and (42) the plasmonic wavelength λ_{spp} is dependent on the real part $\text{Re}\{k_{\text{spp}}\}$, while the propagation length L is dependent on the imaginary part $\text{Im}\{k_{\text{spp}}\}$.

$$\lambda_{\text{spp}} = \frac{2\pi}{\text{Re}\{k_{\text{spp}}\}}, \tag{41}$$

$$L = \frac{1}{2\,\text{Im}\{k_{\text{spp}}\}}. \tag{42}$$

We find the complex wave vector as per the dispersion equation for SPP waves on graphene [83]:

$$-i\frac{\sigma^g}{\omega\varepsilon_0} = \frac{\varepsilon_1 + \varepsilon_2 \coth(k_{spp}d)}{k_{spp}}. \tag{43}$$

Here, σ^g is the conductivity of graphene, ε_1 is the relative permittivity of the dielectric above graphene (air), ε_2 is the relative permittivity of the dielectric below graphene (silicon dioxide), and d is the separation between graphene and the metallic ground plane. The conductivity model for graphene is obtained using the Kubo formalism [84] [85], given by the following equations:

$$\sigma^g = \sigma^g_{intra} + \sigma^g_{inter}, \tag{44}$$

$$\sigma^g_{intra} = i\frac{2e^2}{\pi\hbar^2}\frac{k_B T}{\omega + i\tau_g^{-1}} \ln\left[2\cosh\left(\frac{E_F}{2k_B T}\right)\right], \tag{45}$$

$$\sigma^g_{inter} = \frac{e^2}{4\hbar}\left[H(\frac{\omega}{2}) + i\frac{4\omega}{\pi}\int_0^\infty \frac{G(\epsilon) - G(\omega/2)}{\omega^2 - 4\epsilon^2} d\epsilon\right], \tag{46}$$

and

$$G(a) = \frac{\sinh(\hbar a/k_B T)}{\cosh(E_F/k_B T) + \cosh(\hbar a/k_B T)}. \tag{47}$$

where $\omega = 2\pi f$ is the angular frequency, $\hbar$ is the reduced Planck's constant, e is the electron charge, k_B is the Boltzmann constant, T is the temperature, E_F refers to the Fermi energy of the graphene sheet, and τ_g is the relaxation time of electrons in graphene. The intrinsic properties of graphene, among them the relaxation time, are set as per numerous experimental characterizations of graphene [86].

In such a setup, by changing the Fermi energy of the graphene layer (i.e., the highest energy level occupied by electrons in graphene), for example, by means of electrostatic bias, the SPP wave propagation speed is modified. A change in propagation speed leads to a change in phase of the SPP wave at the output of the stub. Due to the nonlinear nature of these equations, a numerical analysis is required to derive stub dimensions so as to establish a phase delay of 2π radians, with minimal power dissipation across the graphene layer.

3. Joint Design: The hybrid element is obtained by combining the metallic patch and the graphene stub. The metallic patch converts the resonant incident wave to an electrical current, generating SPP waves which propagate across the graphene stub. The SPP wave travels across the length of the graphene stub and back towards the patch, before being radiated back as an EM wave.

Following the transmission line theory of graphene [35], it is understood that changing the Fermi energy of graphene nano-ribbons causes a change in the characteristic impedance. Therefore a mismatch at the metal–graphene interface is expected. However, in the absence of active port elements, the mismatch cannot be studied and accounted for. Instead, a numerical analysis is performed to determine the jointly optimized design. Figure 36a shows a schematic of the final design; with the geometry optimized as per the principle outlined. The dimensions of the hybrid element are summarized in Table 3.

Table 3: Hybrid Element Dimensions

Substrate thickness	2.3 µm
Substrate permittivity	$4\varepsilon_0$
Patch width	63.2 µm
Patch length	49.94 µm
Stub length	15 µm
Stub width	10 µm
Inlet width	9 µm
Inlet length	18 µm
Graphene relaxation time	1 ps

Reflectarray Design and Principle The reflectarray is designed following conventional array theory. The centre to centre separation between the elements is kept at $\lambda_0/2$. This spacing minimizes mutual coupling effects without creating grating lobes [69]. Therefore, mutual coupling effects are negligible. The hybrid reflectarray is presented in Fig. 36b. It is seen that the reflectarray is excited by an external source. Each element of the array is designed to have a certain beamforming weight, assigned through the application of a codebook. The resultant beam from the complete superposition of all the weighted elements is steered to the desired direction (θ, ϕ).

For the planar array in Fig. 36b, to direct an incident wave with free-space wavenumer of k_0 towards a direction $(\theta,\ \phi)$, the progressive phase delay between the elements separated by a distance d needs to be Φ_{RA}, where

$$\Phi_{RA} = k_0(R_i - d \sin\theta(x_i \cos\phi + y_i \sin\phi)). \tag{48}$$

The correction term $k_0 R_i$ is added to account for the incremental inherent phase delay from the incidence angle of the beam. When the incoming wave is broadside, the correction term is rendered void.

Reflectarray Control

1. Codebook Design: To implement the required phase delay of each element at position n, m of the array in Fig. 36b as per Eq. (48), a codebook is defined, composed of effective weights of $W_{n,m}$, corresponding to the n, m element. $W_{n,m}$ is of the form Ae^{iB}, where A represents the magnitude of signal strength, and B represents the relative phase. The reflectarray is intended for phase control. Thus, it is clear that for a complete continuous beamformed array, the weights required are of the form

$$W_{codebook} \in [1e^{i0}, 1e^{i2\pi}]. \tag{49}$$

The application of the derived codebook to the reflectarray results in the reflection of the incident wave in the particular desired direction. In the hybrid array, the codebook is applied by varying the Fermi energy of the graphene stub $EF_{stub_{n,m}}$. Thus, the effective complex weight $W_{n,m}$ is mapped to a particular stub Fermi energy of that element.

$$W_{n,m} \mapsto EF_{stub_{n,m}}. \tag{50}$$

2. Codebook Application: To implement the codebook, the relation between the Fermi energy of the stub and the relative phase delay is required. To develop this, the variation of the electric field amplitude at the output of the stub is found as a function of the Fermi energy of the stub, when transmission mode is considered. This relation is presented in Fig. 37. It is seen that at different Fermi energy levels (all within the common range between 0.1 and 1 eV [87]), the corresponding output fields will exhibit a phase difference exceeding π radians. In reflection, the phase difference is doubled, and therefore complete phase control with 2π radians is possible.

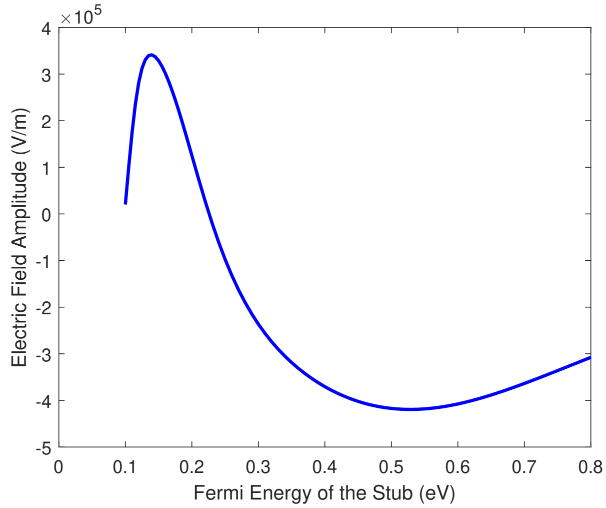

Fig. 37: Amplitude of the electric field at the output of the stub as the Fermi energy of the graphene-based stub is varied.

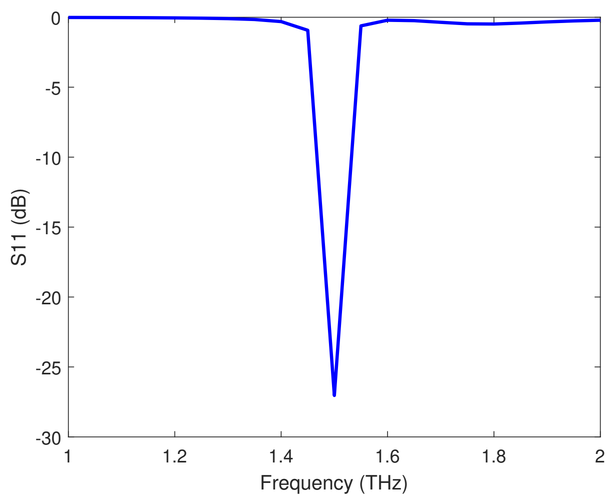

Fig. 38: Frequency response of the hybrid element. Resonance is observed at 1.5 THz.

Results In this section, we numerically investigate the performance of the single element and reflectarray, in terms of the the phase control and beamforming capabilites, respectively. Considering the computational cost of the numerical simulations, we restrict our analyses to a linear array. In the lack of mutual coupling effects as in our design, a planar array can be simplified to a combination of two linear arrays [69], and therefore the analyses presented are sufficient to characterize performance metrics.

1. Single Element Efficiency and Control:

Figure 38 represents the relationship between the S11 parameter and the operating frequency of the hybrid element. At 1.5 THz, the S11 parameter is -27 dB, indicating resonance.

The derived relation between effective phase delay and Fermi energy of the stub is presented in Fig. 39. It is seen that within the common range of Fermi energies, complete phase control is possible.

The magnitude of reflection from the hybrid element is presented in Fig. 40, benchmarked to the signal strengths of metallic and graphene patches, all resonant at 1.5 THz. The metallic patch has the strongest signal reflection, albeit without beamforming support. The hybrid element has slight signal power attenuation due to power dissipation across the graphene stub while supporting total phase control for beamforming. In the case of the graphene only patch, a severely truncated reflecting signal is observed, due to the SPP-EM

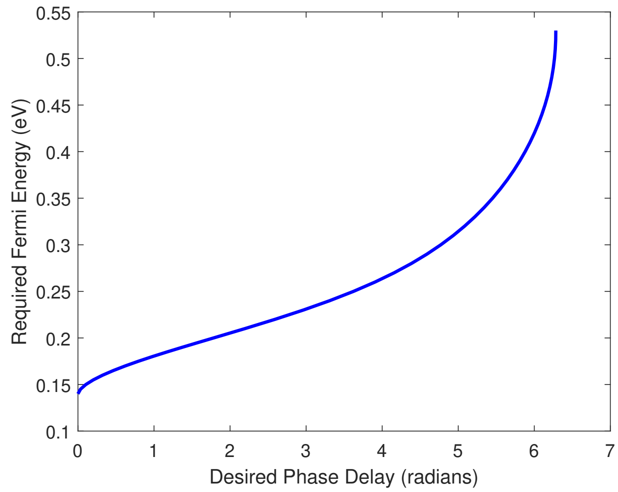

Fig. 39: The relation between the desired phase delay and the required Fermi energy of the graphene-based stub of the element.

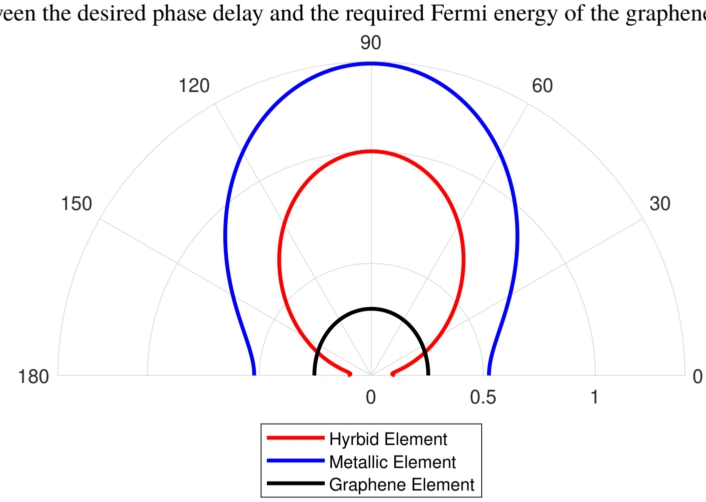

Fig. 40: A comparison between the normalized reflected power from the three different element designs.

mismatch.

2. Reflectarray Beamforming Analysis To assess the dynamic beamforming capability of the reflectarray, a 4×1 reflectarray is analyzed. Figure 41 presents the resultant far-field radiation patterns of the reflected beam obtained from the implementation of the four different codebooks $C0$, $C1$, $C2$ and $C3$, designed to reflect a normal incident beam towards $(\theta, \phi) = (0°,0°)$, $(0°,15°)$, $(0°,30°)$, and $(0°,45°)$, respectively. Table. 4 presents the derived codebooks. It is seen that the hybrid reflectarray successfully reflects the beam in the intended directions.

Table 4: The Derived Codebooks

Codebooks	Fermi Energy of Stubs			
	$EF_{stub_{0,0}}$	$EF_{stub_{1,0}}$	$EF_{stub_{2,0}}$	$EF_{stub_{3,0}}$
$C0$	0.5 eV	0.5 eV	0.5 eV	0.5 eV
$C1$	0.14 eV	0.176 eV	0.198 eV	0.212 eV
$C2$	0.14 eV	0.197 eV	0.232 eV	0.3 eV
$C3$	0.14 eV	0.208 eV	0.287 eV	0.159 eV

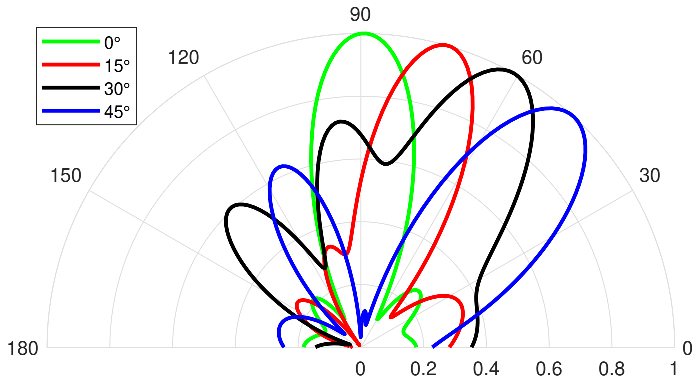

Fig. 41: The far-field radiation patterns of the reflected beam from the application of the codebooks in Table 4 to a 4×1 reflectarray.

4.2.2 Fabrication and Experimental Characterization

In the latest phase of this program, we modified our approach to the graphene/metal hybrid antenna. This is informed by our results from the prior year, which revealed significant challenges to control of the array. Our progress on this problem is described below.

Improved hybrid antenna design In our earlier work, we had fabricated metallic patch antennas directly on a SiO_2 surface coated with continuous graphene. The THz spectra showed a weakening of the signal due to the softened boundary condition at the metal/graphene interface. Moreover, modulation of the graphene via gating proved very difficult, due to the large parasitic capacitance caused by the large graphene area. For this reason, we modified the design such that graphene will serve as the stub of a metal patch antenna. Changing the Fermi energy of this graphene stub should allow us to modulate the phase, making electrostatic beam steering possible.

To confirm the design parameters and test the spectroscopic setup, we first fabricated an all-metal antenna array with fixed-length stubs. This design, shown in Fig. 42a, should direct the reflected beam 90 degrees from the incident angle (10 deg from normal). The corresponding THz spectrum is shown in Fig. 42b. A clear decrease in reflectance relative to the bare substrate is visible at approximately 1.2 THz. This feature is absent when the array is rotated by 90 degrees, confirming the feature is due to the reflectarray. We note that the array was designed for a response at 1.5 THz, which differs from the observed response at 1.2 THz. This disagreement will inform our simulations, allowing us to choose better values when estimating parameters, thus producing more accurate results in future simulations.

While the current funding has expired, we continue to work on this technology and are currently focused on integrating the graphene stubs and metal antennas to realize the hybrid reflectarray structure.

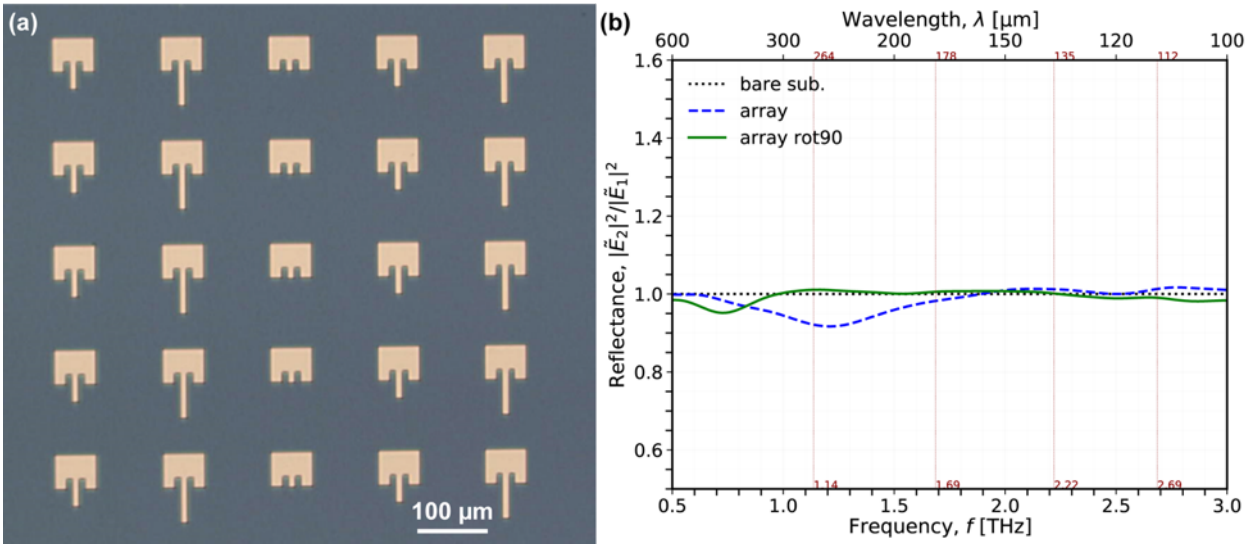

Fig. 42: (a) Optical micrograph of the phase-delay metallic antenna array.(b) Experimentally measured THz spectrum of the metallic array.

5 Summary of Accomplishments

5.1 Papers published and submitted

Peer-reviewed Journals

1. A. Singh, M. Andrello, N. Thawdar and J. M. Jornet, *"Design and Operation of a Graphene-basedPlasmonic Nano-antenna Array for Communicationin the Terahertz Band,"* submitted to IEEE Journal of Selected Areas in Communications (JSAC), 2019.
2. A. Singh, M. Andrello, F. Vandrevala, A. Jaiswal, N. Thawdar, E. Einarsson and J. M. Jornet, *"Design and Operation of a Smart Hybrid Graphene-Metal Reflectarray for THz Communication,"* submitted to IEEE Journal of Selected Areas in Communications (JSAC), 2019.
3. F. Vandrevala and E. Einarsson, *"Origin of pseudo-dispersion in non-dispersive media by terahertz time-domain spectroscopy,"* **Optics Express,** vol. 27, no. 23, pp. 33537–33542, 2019.
4. M. Nafari, G. R. Aizin and J. M. Jornet, *"Plasmonic HEMT Terahertz Transmitter based on the Dyakonov-Shur Instability: Performance Analysis and Impact of Nonideal Boundaries,"* **Physical Review Applied,** vol. 10, no. 6, pp. 064025, December 2018.
5. J. Ma, R. Shrestha, J. Adelberg, C.-Y. Yeh, Z. Hossain, E. Knightly, J. M. Jornet, and D. M. Mittleman, *"Security and eavesdropping in terahertz wireless links,"* **Nature,** vol. 563, no. 7729, pp. 89-93, November 2018.
6. F. Vandrevala and E. Einarsson, *"Decoupling substrate thickness and refractive index measurement in THz time-domain spectroscopy,"* **Optics Express,** vol. 26 no. 2, pp. 1697-1702, 2018.
7. A. Karmakar, F. Vandrevala, F. Gollier, M. A. Philip, S. Shahi, and E. Einarsson, *"Approaching completely continuous centimeter-scale graphene by copolymer-assisted transfer,"* **RSC Advances,** vol. 8 no. 4, pp. 1725-1729, 2018.
8. I. F. Akyildiz, J. M. Jornet and M. Pierobon, *"Nanonetworks,"* in **Encyclopedia of Wireless Networks (Springer),** X. (Sherman) Shen, X. Lin, and K. Zhang, Eds. Cham: Springer International Publishing, 2018.
9. C. Han, J. M. Jornet and I. F. Akyildiz, *"Nanoscale Terahertz Communications,"* in **Encyclopedia of Wireless Networks (Springer),** X. (Sherman) Shen, X. Lin, and K. Zhang, Eds. Cham: Springer International Publishing, 2018.

Peer-reviewed Conferences

1. A. Singh, M. Andrello, E. Einarsson, N. Thawdar and J. M. Jornet, *"Design and Operation of a Smart Graphene-Metal Hybrid Reflectarray at THz Frequencies,"*, to appear in **Prof. of the 14th European Conference on Antennas and Propagation (EuCAP) 2020**, Copenhagen, Denmark, March 2020.
2. A. Jaiswal, A. Singh, F. Vandrevala, J. M. Jornet, and E. Einarsson, *"Hybrid Graphene/Metal Antenna Arrays for Terahertz Communications,"* **Poster Presentation, 2019 Materials Research Society Fall Meeting.**, Boston, USA, December 2019.
3. B. Barut, G. R. Aizin, E. Einarsson, J. M. Jornet, T. Sugaya and J. P. Bird, *"Realizing Asymmetric Boundary Conditions for Plasmonic THz Wave Generation in HEMTs,"* in **Proc. of the 2019 44th International Conference on Infrared, Millimeter, and Terahertz Waves (IRMMW-THz),** Paris, France, September 2019.

4. B. Barut, E. Einarsson, J. M. Jornet, J. P. Bird, G. R. Aizin, and T. Sugaya, *"Realizing asymmetric boundary conditions for plasmonic THz wave generation in HEMTs,"* **Contributed oral presentation, EDISON21 (the 21st International Conference on Electron Dynamics in Semiconductors, Optoelectronics and Nanostructures),** Nara, Japan, July 2019.

5. E. Einarsson, A. Karmakar, F. Vandrevala, A. Singh, and J. M. Jornet, *"Graphene-based reflectarrays for wireless terahertz communications,"* **Invited oral presentation, 56th Fullerenes–Nanotubes–Graphene General Symposium,** Tokyo, Japan, March 2019.

6. E. Einarsson, F. Vandrevala, A. Karmakar, A. Singh, and J. M. Jornet, *"Hybrid graphene/metal reflectarray for THz communications,"* **Invited oral presentation, CIAiS International Symposium 2019,** Tokyo, Japan, March 2019.

7. B. Barut, E. Einarsson, J. M. Jornet, and J. P. Bird, G. R. Aizin, and T. Sugaya, *"Realizing asymmetric boundary conditions for plasmonic THz wave generation in HEMTs,"* **Contributed poster presentation, WINDS 2018 (the 2018 International Workshop on Innovative Nanoscale Devices and Systems),** Hawaii, November 2018.

8. I. Mehdi, J. V. Siles, C. Chen, J. M. Jornet, *"THz Technology for Space Communications,"* in **Proc. of 2018 Asia-Pacific Microwave Conference (APMC)**, Kyoto, Japan, November 2018. (Invited)

9. F. Vandrevala, A. Karmakar, J. M. Jornet and E. Einarsson, *"Graphene Characterization using Time-Domain Terahertz Spectroscopy for Plasmonic Antenna Design (Poster Presentation),"* in **Proc. of the 5th ACM/IEEE International Conference on Nanoscale Computing and Communications (NanoCom),** Reykjavik, Iceland, September 5-7, 2018.

10. A. Karmakar, F. Vandrevala, A. Singh[a], J. M. Jornet and E. Einarsson, *"Experimental characterization of a hybrid graphene/metal plasmonic antenna array (Poster Presentation),"* in **Proc. of the 5th ACM/IEEE International Conference on Nanoscale Computing and Communications (NanoCom),** Reykjavik, Iceland, September 5-7, 2018.

11. Q. Xia and J. M. Jornet, *"Leveraging Antenna Side-lobe Information for Expedited Neighbor Discovery in Directional Terahertz Communication Networks,"* in **Proc. of IEEE Vehicular Technology Conference (VTC)-Spring,** Porto, Portugal, June 2018.

12. J. P. Bird, J. M. Jornet, E. Einarsson and G. Aizin, *"Prospects for the Application of 2-Dimensional Materials to Terahertz-Band Communications,"* in **Proc. of the 4th ACM International Conference on Nanoscale Computing and Communications (NanoCom),** pp. 1-2, Arlington, Virginia, September 2017. **(Invited)**.

13. Z. Hossain, C. Nicoletti and J. M. Jornet, *"Stochastic Multipath Channel Modeling and Power Delay Profile Analysis for Terahertz-band Communication,"* in **Proc. of the 4th ACM International Conference on Nanoscale Computing and Communications (NanoCom),** pp. 1-6, Arlington, Virginia, September 2017.

14. J. M. Jornet, *"Hybrid Graphene/semiconductor Technology for Ultra-broadband Terahertz Communications,"* in **Proc. of the 42 International Conference on Infrared, Millimeter and Terahertz Waves (IRMMW-THz),** pp. 1-2, Cancun, Mexico, August 2017. **(Invited)**

15. M. Nafari, G. Aizin and J. M. Jornet, *"Numerical Studies of the Plasma Wave Instability in Gated Two-dimensional Electron Channels for On-chip THz Signal Generation,"* in **Proc. of the 20th International Conference on Electron Dynamics in Semiconductors, Optoelectronics and Nanostructures (EDISON),** Buffalo, NY, pp.1, July 2017.

16. J. M. Jornet, E. Woo, M. Andrello and N. Thawdar, *"Temporal Dynamics of Frequency-tunable Graphene-based Plasmonic Grating Structures for Ultra-broadband Terahertz Communication,"* in **Proc. of SPIE Defense + Security Conference,** pp. 1-11, Anaheim, CA, April 2017.

17. L. Zakrajsek, D. Pados and J. M. Jornet, *"Design and Performance Analysis of Ultra-massive Multi-carrier Multiple Input Multiple Output Communication in the Terahertz Band,"* in **Proc. of SPIE Defense + Security Conference,** pp. 1-11, Anaheim, CA, April 2017.

18. L. Zakrajsek, E. Einarsson, N. Thawdar, M. Medley and J. M. Jornet, *"Design of Graphene-based Plasmonic Nano-antenna Arrays in the Presence of Mutual Coupling,"* in **Proc. of the 11th European Conference on Antennas and Propagation,** pp. 1-5, Paris, France, March 2017.

19. F. Vandrevala, A. Karmakar, F. Lu, J. M. Jornet and E. Einarsson, *"Extracting Complex Optical Properties of Extremely Thin Materials using Time-domain THz Spectroscopy,"* in Proc. of IRMMW-THz 2016, pp. 1-2, September 2016.

5.2 Major Collaborations

1. **Dr. Ngwe Thawdar, Air Force Research Laboratory, Information Directorate:** The lab is interested in compact, room-temperature, high bandwidth THz transceivers and antennas for ultra-directional ultra-broadband links. In addition to periodic visits during the year, J. M. Jornet and a few of his students have spent several summers at the AFRL as part of the Visiting Faculty Research Program (VFRP) and summer intern program.

2. **Dr. Takeyoshi Sugaya, Research Center for Photovoltaics, National Institute of Advanced Industrial Science and Technology (AIST), Japan:** He has provided the team with InGaAs quantum-well material in our experiments.

3. **Prof. Susumu Komiyama, National Institute of Information and Communications technology (NICT), Japan:** He has provided the team with the *p*-type Ge detectors that are being utilized to characterize the emission from the THz source.

4. **Jose V. Siles, NASA Jet Propulsion Laboratory:** For decades, NASA JPL has been developing THz technologies for Earth and remote sensing. More recently, the THz band has also been considered for space communications (e.g., between satellites [88]). In collaboration with Jose, our group has demonstrated fully-functional ultra-broadband THz communication links.

5.3 Student Support

1. B. Barut, Ph.D. student, Advisor: J. P. Bird, expected to graduate in March 2020.

2. R. Dixit, Ph.D. student, Advisor: J. P. Bird, expected to graduate in March 2021.

3. A. Jaiswal, Ph.D. student, Advisor: E. Einarsson, expected to graduate in 2021.

4. A. Karmakar, Ph.D. student, Advisor: E. Einarsson, graduated in February 2019, now a postdoctoral scholar at Okinawa Institute of Science and Technology, Japan.

5. M. Nafari, Ph.D. student, Advisor: J. M. Jornet, graduated in August 2018, now a Senior Technology and Integration Engineer at GLOBAL FOUNDRIES.

6. A. Singh, Ph.D. student, Advisor: J. M. Jornet, expected to graduate in May 2021.

7. F. Vandrevala, Ph.D. student, Advisor: E. Einarsson, graduated in September 2019, now an Assistant Professor of Teaching in the Department of Electrical Engineering at the University at Buffalo.

5.4 Talks, Seminars and Tutorials

1. *"Terahertz Communications: A Physical-Layer Perspective,"* **Half-day Tutorial at the 2020 IEEE International Conference on Communications (ICC)**, June 2020.

2. *"Conquering the Terahertz Band: From Theory to Practice,"* **mmWave Coalition TechForum,** USA, January 2020.

3. *"Terahertz Communications: From Nanomaterials to Ultra-broadband Networks,"* **Keynote Speech at the International Conference on Electrical and Computer Technologies and Applications (ICECTA 2019),** Dubai, UAE, November 2019.

4. *"Conquering the Spectrum: THz and Beyond,"* **Inauguration of the Institute for the Wireless Internet of Things** at Northeastern University, Boston, MA, October 18, 2019.

5. *"Conquering the Terahertz Band: From Theory to Practice,"* **43rd Wireless World Research Forum (WWRF) Meeting,** London, UK, October 9-11, 2019.

6. *"Terahertz Communications: From Nanomaterials to Ultra-broadband Networks,"* Seminar, **Queen Mary University of London,** London, UK, October 10, 2019.

7. *"Enabling Terahertz Communication Networks: From Theory to Practice,"* **Workshop on Terahertz Devices, Circuits and Systems: from fundamentals to applications, European Microwave Week,** Paris, France, October 2019.

8. *"Closing the Terahertz Gap for 6G Systems,"* **Advanced Wireless Research Roundtable,** Washington DC, USA, September 2019.

9. *"Ultra-broadband Communications at Terahertz Frequencies,"* **Rump Session: FCC Opens Above 95-GHz Spectrum: Beyond 5G & Other Applications** , 2019 IEEE International Microwave Symposium (IMS), Boston, MA, USA, June 2019.

10. *"Ultra-broadband Networking in the Terahertz Band and Beyond,"* **Wireless Research Roundtable 2019,** National Instruments, Shanghai, China, May 2019.

11. *"Terahertz Communications: From Nanomaterials to Ultra-broadband Networks,"* **Distinguished Seminar, Institute for the Wireless Internet of Things,** Northeastern University, Boston, MA, USA, January 2019.

12. *"Terahertz Communications: Antennas and Propagation,"* **FCC Technological Advisory Council**, Washington DC, USA, November 2018.

13. *"Towards Ultra-broadband Terahertz Communication Networks,"* **Seminar, NASA Jet Propulsion Laboratory (JPL),** Pasadena, CA, USA, October 2018.

14. *"Terahertz Communications: Challenges and Opportunities for Defense and Commercial Applications,"* **Panel Moderator, IEEE Military Communications Conference (MILCOM),** LA, CA, USA, October 2018.

15. *"Terahertz Communications: From Nanomaterials to Ultra-broadband Networks,"* **Invited Seminar, NYU Wireless,** NYC, NY, USA, September 2018.

16. J. M. Jornet, *"Hybrid Graphene/semiconductor Technology for Terahertz Communications,"* **Invited Talk, IEEE Research and Applications of Photonics In Defense Conference (RAPID),** Miramar Beach, FL, USA, August 2018.

17. J. M. Jornet, *“Terahertz Communications: A Key Enabling Technology for Beyond 5G Systems,"* **Half-day Tutorial at IEEE 25th International Conference on Telecommunication (ICT) 2018,** Saint Malo, France, June 26-28, 2018.

18. J. M. Jornet, *“Graphene Plasmonics and Nano-Communications in the THz Band,"* **2h Lecture at the 2018 European School of Antennas on Terahertz Technology and Applications,** Universitat Politecnica de Catalunya, Barcelona, Spain, June 2018.

19. J. M. Jornet, *“Terahertz Communications: A Key Enabling Technology for Beyond 5G Systems,"* **Half-day Tutorial at IEEE International Conference on Communications (ICC) 2018,** Kansas City, MO, USA, May 20, 2018.

20. J. M. Jornet, *“Terahertz Communications: Ultra-broadband Transceivers, Antennas and Propagation,"* **Half-day Tutorial at 12th European Conference on Antennas and Propagation (EuCAP) 2018,** London, UK, April 9, 2018.

21. J. M. Jornet, *“Terahertz Communications: A Key Enabling Technology for Beyond 5G Systems,"* **Keynote Speech at the Third International Conference on Wireless Communications Signal Processing and Networking (WiSPNET),** Chennai, India, March 22, 2018.

22. J. M. Jornet, *“The Internet of Nano-Things: From Nanomaterials to Macrosystems,* **Seminar in the Barcelona School of Telecommunications Engineering (ETSETB), Universitat Politecnica de Catalunya,** Barcelona, Spain, January 18, 2018.

23. J. M. Jornet, *“Ultra-broadband Wireless Communications in the Terahertz Band (and Beyond),"* **Seminar in the Departament d’Enginyeria Informatica i Matematiques, Universitat Rovira i Virgili,** Tarragona, Spain, January 10, 2018.

24. J. M. Jornet, *“Terahertz Communications: A Key Enabling Technology for Beyond 5G Systems,"* **Seminar in the Department of Electrical and Computer Engineering, Michigan State University,** Lansing, MI, USA, November 29, 2017.

25. J. M. Jornet, *“Terahertz Communications: A Key Enabling Technology for Beyond 5G Systems,"* **Seminar in the Department of Electrical and Computer Engineering, Northeastern University,** Boston, MA, USA, November 10, 2017.

26. J. M. Jornet, *“Terahertz Communications: A Key Enabling Technology for Beyond 5G Systems,"* **Keynote Speaker at the 2nd Workshop on THz Communications (THZCOM),** in conjunction with the 9th International Congress on Ultra Modern Telecommunications and Control Systems (ICUMT), Munich, Germany, November 8, 2017.

27. J. M. Jornet, *“Ultra-broadband Networking at Terahertz Frequencies,"* **IEEE 802.15 WPAN Terahertz Interest Group, IEEE 802 LAN/MAN Standards Committee Plenary Meeting,** Orlando, FL, November 6, 2017.

28. J. M. Jornet, *“Ultra-broadband Communication Networks in the Terahertz Band (and Beyond),"* **Department of Information Engineering, Electronics and Telecommunications, University of Rome, La Sapienza,** Roma, Italy, October 12, 2017.

29. J. M. Jornet, *“Ultra-broadband Terahertz Communications,"* Colloquium on 5G Technologies, **AFRL/RI**, Rome, NY, July 27, 2017.

30. J. M. Jornet, *“Ultra-broadband Communications in the Terahertz Band (and beyond),"* Seminar in the School of Computer Science and Engineering, **University of New South Wales,** Sydney, Australia, June 6, 2017.

31. J. M. Jornet, *"Future Enablers for the Security of IoT and Cyber Physical Systems,"* Panel at the **Proc. of SPIE Defense + Security Conference,** Anaheim, CA, April 2017.
32. J. M. Jornet, *"Ultra-broadband Wireless Communication Networks in the Terahertz Band (and Beyond),"* Seminar at **Intel Labs,** Hillsboro, OR, November 2016.
33. J. M. Jornet, *"Hybrid Graphene/semiconductor Plasmonic Technology for Ultra-broadband THz Communications,"* Keck Center Meeting, **Brown University,** Providence, RI, October 2016.

References

[1] Cisco, "Cisco visual networking index: Global mobile data traffic forecast update, 2017–2022," *White Paper*, Feb. 2018.

[2] S. Cherry, "Edholm's law of bandwidth," *IEEE Spectrum*, vol. 41, no. 7, pp. 58–60, Jul. 2004.

[3] Nokia Networks, "LTE Advanced Pro, pushing LTE capabilities towards 5G," Tech. Rep., 2015.

[4] T. Rappaport, J. Murdock, and F. Gutierrez, "State of the art in 60-GHz integrated circuits and systems for wireless communications," *Proceedings of the IEEE*, vol. 99, no. 8, pp. 1390–1436, Aug. 2011.

[5] M. A. Khalighi and M. Uysal, "Survey on free space optical communication: A communication theory perspective," *IEEE Communications Surveys Tutorials*, vol. 16, no. 4, pp. 2231–2258, Fourthquarter 2014.

[6] J. Federici and L. Moeller, "Review of terahertz and subterahertz wireless communications," *Journal of Applied Physics*, vol. 107, no. 11, p. 111101, 2010.

[7] H.-J. Song and T. Nagatsuma, "Present and future of terahertz communications," *IEEE Transactions on Terahertz Science and Technology*, vol. 1, no. 1, pp. 256–263, 2011.

[8] I. F. Akyildiz, J. M. Jornet, and C. Han, "Terahertz band: Next frontier for wireless communications," *Physical Communication (Elsevier) Journal*, vol. 12, pp. 16–32, Sep. 2014.

[9] T. Kurner and S. Priebe, "Towards THz Communications-Status in Research, Standardization and Regulation," *Journal of Infrared, Millimeter, and Terahertz Waves*, vol. 35, no. 1, pp. 53–62, 2014.

[10] J. M. Jornet and I. F. Akyildiz, "Channel modeling and capacity analysis of electromagnetic wireless nanonetworks in the terahertz band," *IEEE Transactions on Wireless Communications*, vol. 10, no. 10, pp. 3211–3221, Oct. 2011.

[11] J. Ma, R. Shrestha, J. Adelberg, C.-Y. Yeh, Z. Hossain, E. Knightly, J. M. Jornet, and D. M. Mittleman, "Security and eavesdropping in terahertz wireless links," *Nature*, vol. 563, no. 7729, p. 89, 2018.

[12] U. A. Force, "Air force future operating concept: A view of the air force in 2035," Sep. 2015.

[13] K. Sengupta, T. Nagatsuma, and D. M. Mittleman, "Terahertz integrated electronic and hybrid electronic–photonic systems," *Nature Electronics*, vol. 1, no. 12, p. 622, 2018.

[14] A. Nikpaik, A. H. M. Shirazi, A. Nabavi, S. Mirabbasi, and S. Shekhar, "A 219-to-231 ghz frequency-multiplier-based vco with˜ 3% peak dc-to-rf efficiency in 65-nm cmos," *IEEE Journal of Solid-State Circuits*, vol. 53, no. 2, pp. 389–403, 2018.

[15] H. Aghasi, A. Cathelin, and E. Afshari, "A 0.92-thz sige power radiator based on a nonlinear theory for harmonic generation," *IEEE Journal of Solid-State Circuits*, vol. 52, no. 2, pp. 406–422, 2017.

[16] W. R. Deal, K. Leong, A. Zamora, B. Gorospe, K. Nguyen, and X. B. Mei, "A 660 ghz up-converter for thz communications," in *Compound Semiconductor Integrated Circuit Symposium (CSICS), 2017 IEEE*. IEEE, 2017, pp. 1–4.

[17] A. Leuther, A. Tessmann, P. Doria, M. Ohlrogge, M. Seelmann-Eggebert, H. Maßler, M. Schlechtweg, and O. Ambacher, "20 nm metamorphic hemt technology for terahertz monolithic integrated circuits," in *9th IEEE European Microwave Integrated Circuit Conference (EuMIC)*. IEEE, 2014, pp. 84–87.

[18] M. Urteaga, Z. Griffith, M. Seo, J. Hacker, and M. J. Rodwell, "Inp hbt technologies for thz integrated circuits," *Proceedings of the IEEE*, vol. 105, no. 6, pp. 1051–1067, 2017.

[19] I. Mehdi, J. V. Siles, C. Lee, and E. Schlecht, "Thz diode technology: status, prospects, and applications," *Proceedings of the IEEE*, vol. 105, no. 6, pp. 990–1007, 2017.

[20] H.-J. Song, K. Ajito, Y. Muramoto, A. Wakatsuki, T. Nagatsuma, and N. Kukutsu, "Uni-travelling-carrier photodiode module generating 300 ghz power greater than 1 mw," *IEEE Microwave and Wireless Components Letters*, vol. 22, no. 7, pp. 363–365, 2012.

[21] S.-W. Huang, J. Yang, S.-H. Yang, M. Yu, D.-L. Kwong, T. Zelevinsky, M. Jarrahi, and C. W. Wong, "Globally stable microresonator turing pattern formation for coherent high-power thz radiation on-chip," *Physical Review X*, vol. 7, no. 4, p. 041002, 2017.

[22] T. Nagatsuma, G. Ducournau, and C. C. Renaud, "Advances in terahertz communications accelerated by photonics," *Nature Photonics*, vol. 10, no. 6, p. 371, 2016.

[23] Q. Lu, D. Wu, S. Sengupta, S. Slivken, and M. Razeghi, "Room temperature continuous wave, monolithic tunable THz sources based on highly efficient mid-infrared quantum cascade lasers," *Scientific reports*, vol. 6, 2016.

[24] M. Dyakonov and M. Shur, "Shallow water analogy for a ballistic field effect transistor: New mechanism of plasma wave generation by dc current," *Phys. Rev. Lett.*, vol. 71, pp. 2465–2468, Oct. 1993.

[25] W. Knap, J. Lusakowski, T. Parenty, S. Bollaert, A. Cappy, V. Popov, and M. Shur, "Terahertz emission by plasma waves in 60 nm gate high electron mobility transistors," *Applied Physics Letters*, vol. 84, no. 13, pp. 2331–2333, 2004.

[26] S. Boubanga-Tombet, F. Teppe, D. Coquillat, S. Nadar, N. Dyakonova, H. Videlier, W. Knap, A. Shchepetov, C. Gardes, Y. Roelens, S. Bollaert, D. Seliuta, R. Vadoklis, and G. Valusis, "Current driven resonant plasma wave detection of terahertz radiation: Toward the dyakonov-shur instability," *Applied Physics Letters*, vol. 92, no. 21, pp. –, 2008.

[27] A. El Fatimy, S. B. Tombet, F. Teppe, W. Knap, D. Veksler, S. Rumyantsev, M. Shur, N. Pala, R. Gaska, Q. Fareed *et al.*, "Terahertz detection by GaN/AlGaN transistors," *Electronics Letters*, vol. 42, no. 23, pp. 1342–1344, 2006.

[28] S. Boubanga-Tombet, F. Teppe, J. Torres, A. El Moutaouakil, D. Coquillat, N. Dyakonova, C. Consejo, P. Arcade, P. Nouvel, H. Marinchio *et al.*, "Room temperature coherent and voltage tunable terahertz emission from nanometer-sized field effect transistors," *Applied Physics Letters*, vol. 97, no. 26, p. 262108, 2010.

[29] S. Bhardwaj, N. K. Nahar, S. Rajan, and J. L. Volakis, "Numerical analysis of terahertz emissions from an ungated hemt using full-wave hydrodynamic model," *IEEE Transactions on Electron Devices*, vol. 63, no. 3, pp. 990–996, 2016.

[30] T. Otsuji, T. Watanabe, S. Boubanga Tombet, A. Satou, W. Knap, V. Popov, M. Ryzhii, and V. Ryzhii, "Emission and detection of terahertz radiation using two-dimensional electrons in III-V semiconductors and graphene," *IEEE Transactions on Terahertz Science and Technology*, vol. 3, no. 1, pp. 63–71, 2013.

[31] A. K. Geim and K. S. Novoselov, "The rise of graphene," *Nature Materials*, vol. 6, no. 3, pp. 183–191, Mar. 2007.

[32] K. S. Novoselov, V. Fal, L. Colombo, P. Gellert, M. Schwab, K. Kim *et al.*, "A roadmap for graphene," *Nature*, vol. 490, no. 7419, pp. 192–200, 2012.

[33] A. C. Ferrari, F. Bonaccorso, V. Fal'Ko, K. S. Novoselov, S. Roche, P. Bøggild, S. Borini, F. H. Koppens, V. Palermo, N. Pugno *et al.*, "Science and technology roadmap for graphene, related two-dimensional crystals, and hybrid systems," *Nanoscale*, vol. 7, no. 11, pp. 4598–4810, 2015.

[34] J. M. Jornet and I. F. Akyildiz, "Graphene-based plasmonic nano-transceiver for terahertz band communication," in *Proc. of European Conference on Antennas and Propagation (EuCAP)*, 2014.

[35] J. M. Jornet and I. F. Akyildiz, "Graphene-based nano-antennas for electromagnetic nanocommunications in the terahertz band," in *Proc. of 4th European Conference on Antennas and Propagation, EUCAP*, Apr. 2010.

[36] J. M. Jornet and I. F. Akyildiz, "Graphene-based plasmonic nano-antenna for terahertz band communication in nanonetworks," *IEEE JSAC, Special Issue on Emerging Technologies for Communications*, vol. 12, no. 12, pp. 685–694, Dec. 2013.

[37] P. K. Singh, G. Aizin, N. Thawdar, M. Medley, and J. M. Jornet, "Graphene-based plasmonic phase modulator for terahertz-band communication," in *Proc. of the European Conference on Antennas and Propagation (EuCAP)*, 2016.

[38] J. M. Jornet, "Hybrid graphene/semiconductor plasmonic technology for ultra-broadband terahertz communications," in *2017 42nd International Conference on Infrared, Millimeter, and Terahertz Waves (IRMMW-THz)*. IEEE, 2017, pp. 1–2.

[39] J. P. Bird, J. M. Jornet, E. Einarsson, and G. R. Aizin, "Prospects for the application of two-dimensional materials to terahertz-band communications," in *Proceedings of the 4th ACM International Conference on Nanoscale Computing and Communication*. ACM, 2017, p. 28.

[40] M. Nafari, G. R. Aizin, and J. M. Jornet, "Plasmonic hemt terahertz transmitter based on the dyakonov-shur instability: Performance analysis and impact of nonideal boundaries," *Physical Review Applied*, vol. 10, no. 6, p. 064025, 2018.

[41] B. Barut, G. R. Aizin, E. Einarsson, J. M. Jornet, T. Sugaya, and J. P. Bird, "Realizing asymmetric boundary conditions for plasmonic thz wave generation in hemts," in *2019 44th International Conference on Infrared, Millimeter, and Terahertz Waves (IRMMW-THz)*. IEEE, 2019, pp. 1–1.

[42] L. Zakrajsek, E. Einarsson, N. Thawdar, M. Medley, and J. M. Jornet, "Design of graphene-based plasmonic nano-antenna arrays in the presence of mutual coupling," in *Proc. of the 11th European Conference on Antennas and Propagation (EuCAP)*, 2017.

[43] L. M. Zakrajsek, D. A. Pados, and J. M. Jornet, "Design and performance analysis of ultra-massive multi-carrier multiple input multiple output communications in the terahertz band," in *Image Sensing Technologies: Materials, Devices, Systems, and Applications IV*, vol. 10209. International Society for Optics and Photonics, 2017, p. 102090A.

[44] A. Singh, M. Andrello, N. Thawdar, and J. M. Jornet, "Design and operation of a graphene-based plasmonic nano-antenna array for communication in the terahertz band," *IEEE JSAC Special Issue on Multiple Antenna Technologies for Beyond 5G*, Feb. 2020.

[45] A. Singh, M. Andrello, E. Einarsson, N. Thawdar, and J. M. Jornet, "Design and operation of a smart Graphene-Metal hybrid reflectarray at THz frequencies," in *Prof. of the 14th European Conference on Antennas and Propagation (EuCAP 2020)*, Copenhagen, Denmark, Mar. 2020.

[46] A. Singh, M. Andrello, F. Vandrevala, A. Jaiswal, N. Thawdar, E. Einarsson, and J. M. Jornet, "Design and operation of a smart hybrid Graphene-Metal reflectarray for THz communication," *2019 JSAC-SI-RIS (IEEE JSAC Special issue on Wireless Networks Empowered by Reconfigurable Intelligent Surfaces)*, Sep. 2020.

[47] A. Karmakar, F. Vandrevala, F. Gollier, M. A. Philip, S. Shahi, and E. Einarsson, “Approaching completely continuous centimeter-scale graphene by copolymer-assisted transfer,” *RSC Advances*, vol. 8, no. 4, pp. 1725–1729, 2018.

[48] F. Vandrevala, A. Karmakar, J. M. Jornet, and E. Einarsson, “Extracting complex optical properties of ultra-thin conductors using time-domain thz spectroscopy,” in *41st International Conference on Infrared, Millimeter, and Terahertz waves (IRMMW-THz)*. IEEE, 2016, pp. 1–2.

[49] F. Vandrevala and E. Einarsson, “Decoupling substrate thickness and refractive index measurement in thz time-domain spectroscopy,” *Optics express*, vol. 26, no. 2, pp. 1697–1702, 2018.

[50] F. Vandrevala and E. Einarsson, “Origin of pseudo-dispersion in non-dispersive media by terahertz time-domain spectroscopy,” *Optics Express*, vol. 27, no. 23, pp. 33 537–33 542, 2019.

[51] A. Karmakar, F. Vandrevala, A. Singh, J. M. Jornet, and E. Einarsson, “Experimental characterization of a hybrid graphene/metal plasmonic antenna array,” in *Proc. of the 5th ACM/IEEE International Conference on Nanoscale Computing and Communications (NanoCom)*, 2018.

[52] F. Vandrevala, A. Karmakar, J. M. Jornet, and E. Einarsson, “Graphene characterization using time-domain terahertz spectroscopy for plasmonic antenna design,” in *Proceedings of the 5th ACM International Conference on Nanoscale Computing and Communication*. ACM, 2018, p. 35.

[53] A. L. Fetter, “Electrodynamics of a layered electron gas. i. single layer,” *Annals of Physics*, vol. 81, no. 2, pp. 367–393, 1973.

[54] A. Jungel, *Quasi-hydrodynamic semiconductor equations*. Birkhauser Verlag, 2001.

[55] K. S. Novoselov, A. K. Geim, S. V. Morozov, D. Jiang, Y. Zhang, S. V. Dubonos, I. V. Grigorieva, and A. A. Firsov, “Electric Field Effect in Atomically Thin Carbon Films,” *Science*, vol. 306, no. 5696, pp. 666–669, 2004.

[56] R. Bistritzer and A. MacDonald, “Hydrodynamic theory of transport in doped graphene,” *Physical Review B*, vol. 80, no. 8, p. 085109, 2009.

[57] G. Uhlenbeck and G. Ford, *Lectures in statistical mechanics*, ser. Lectures in applied mathematics. American Mathematical Society, 1963.

[58] D. Svintsov, V. Vyurkov, S. Yurchenko, T. Otsuji, and V. Ryzhii, “Hydrodynamic model for electron-hole plasma in graphene,” *Journal of Applied Physics*, vol. 111, no. 8, p. 083715, 2012.

[59] I. Llatser, C. Kremers, A. Cabellos-Aparicio, J. M. Jornet, E. Alarcon, and D. N. Chigrin, “Graphene-based nano-patch antenna for terahertz radiation,” *Photonics and Nanostructures - Fundamentals and Applications*, vol. 10, no. 4, pp. 353–358, Oct. 2012.

[60] M. Tamagnone, J. S. Gomez-Diaz, J. R. Mosig, and J. Perruisseau-Carrier, “Reconfigurable terahertz plasmonic antenna concept using a graphene stack,” *Applied Physics Letters*, vol. 101, no. 21, p. 214102, 2012.

[61] M. Aldrigo, M. Dragoman, and D. Dragoman, “Smart antennas based on graphene,” *Journal of Applied Physics*, vol. 116, no. 11, 2014.

[62] I. F. Akyildiz and J. M. Jornet, “Realizing ultra-massive MIMO (1024×1024) communication in the (0.06–10) terahertz band,” *Nano Communication Networks*, vol. 8, pp. 46–54, 2016.

[63] W. Tan, Y. Sun, Z.-G. Wang, and H. Chen, “Manipulating electromagnetic responses of metal wires at the deep subwavelength scale via both near-and far-field couplings,” *Applied Physics Letters*, vol. 104, no. 9, p. 091107, 2014.

[64] H. A. Haus, *Waves and fields in optoelectronics*. Prentice-Hall,, 1984.

[65] E. Van Lil and A. Van de Capelle, “Transmission line model for mutual coupling between microstrip antennas,” *IEEE Transactions on antennas and propagation*, vol. 32, no. 8, pp. 816–821, 1984.

[66] M. Malkomes, “Mutual coupling between microstrip patch antennas,” *Electronics Letters*, vol. 18, pp. 520–522, 1982.

[67] E. Penard and J.-P. Daniel, “Mutual coupling between microstrip antennas,” *Electronics Letters*, vol. 18, pp. 605–607, 1982.

[68] A. Derneryd, “A theoretical investigation of the rectangular microstrip antenna element,” *IEEE Transactions on Antennas and Propagation*, vol. 26, no. 4, pp. 532–535, 1978.

[69] C. A. Balanis, *Antenna theory: analysis and design*. John Wiley & Sons, 2005.

[70] L. Zakrajsek, E. Einarsson, N. Thawdar, M. Medley, and J. M. Jornet, “Lithographically defined plasmonic graphene antennas for terahertz-band communication,” *IEEE Antennas and Wireless Propagation Letters*, vol. 15, pp. 1553–1556, 2016.

[71] P. U. Jepsen, U. Møller, and H. Merbold, “Investigation of aqueous alcohol and sugar solutions with reflection terahertz time-domain spectroscopy,” *Opt. Express*, vol. 15, no. 22, pp. 14 717–14 737, Oct 2007. [Online]. Available: http://www.opticsexpress.org/abstract.cfm?URI=oe-15-22-14717

[72] Y. Zhou, Y. E, L. Zhu, M. Qi, X. Xu, J. Bai, Z. Ren, and L. Wang, “Terahertz wave reflection impedance matching properties of graphene layers at oblique incidence,” *Carbon*, vol. 96, pp. 1129 – 1137, 2016. [Online]. Available: http://www.sciencedirect.com/science/article/pii/S0008622315303730

[73] P. R. Whelan, K. Iwaszczuk, R. Wang, S. Hofmann, P. Bøggild, and P. U. Jepsen, "Robust mapping of electrical properties of graphene from terahertz time-domain spectroscopy with timing jitter correction," *Opt. Express*, vol. 25, no. 3, pp. 2725–2732, Feb 2017. [Online]. Available: http://www.opticsexpress.org/abstract.cfm?URI=oe-25-3-2725

[74] N. V. Smith, "Classical generalization of the drude formula for the optical conductivity," *Phys. Rev. B*, vol. 64, p. 155106, Sep 2001. [Online]. Available: https://link.aps.org/doi/10.1103/PhysRevB.64.155106

[75] T. Ando, A. B. Fowler, and F. Stern, "Electronic properties of two-dimensional systems," *Reviews of Modern Physics*, vol. 54, no. 2, p. 437, 1982.

[76] G. R. Aizin and G. C. Dyer, "Transmission line theory of collective plasma excitations in periodic two-dimensional electron systems: Finite plasmonic crystals and tamm states," *Physical Review B*, vol. 86, no. 23, p. 235316, 2012.

[77] M. Cheremisin and G. Samsonidze, "Dyakonov-shur instability in a ballistic field-effect transistor with a spatially nonuniform channel," *Semiconductors*, vol. 33, no. 5, pp. 578–585, 1999.

[78] A. Aste and R. Vahldieck, "Time-domain simulation of the full hydrodynamic model," *arXiv preprint physics/0312021*, 2003.

[79] A. Z. Elsherbeni and V. Demir, *The finite-difference time-domain method for electromagnetics with MATLAB simulations*. The Institution of Engineering and Technology, 2016.

[80] A. Taflove and S. C. Hagness, *Computational electrodynamics*. Artech house, 2005.

[81] J. Hu and L. Wang, "An asymptotic-preserving scheme for the semiconductor boltzmann equation toward the energy-transport limit," *Journal of Computational Physics*, vol. 281, pp. 806–824, 2015.

[82] N. Payam, Y. Fan, and A. Z. Elsherbeni, *Reflectaray Antennas: Theory, Designs, and Applications*. Wiley-IEEE Press, 2018.

[83] V. Ryzhii, "Terahertz plasma waves in gated graphene heterostructures," *Japanese journal of applied physics*, vol. 45, no. 9L, p. L923, 2006.

[84] G. W. Hanson, "Dyadic Green's functions and guided surface waves for a surface conductivity model of graphene," *Journal of Applied Physics*, vol. 103, no. 6, p. 064302, 2008.

[85] L. Falkovsky and A. A. Varlamov, "Space-time dispersion of graphene conductivity," *The European Physical Journal B*, vol. 56, pp. 281–284, 2007.

[86] A. S. Mayorov, R. V. Gorbachev, S. V. Morozov, L. Britnell, R. Jalil, L. A. Ponomarenko, P. Blake, K. S. Novoselov, K. Watanabe, T. Taniguchi *et al.*, "Micrometer-scale ballistic transport in encapsulated graphene at room temperature," *Nano letters*, vol. 11, no. 6, pp. 2396–2399, 2011.

[87] H. Ramamoorthy, R. Somphonsane, J. Radice, G. He, C. Kwan, and J. P. Bird, "Freeing graphene from its substrate: Observing intrinsic velocity saturation with rapid electrical pulsing," *Nano letters*, vol. 16, no. 1, pp. 399–403, 2015.

[88] I. Mehdi, J. V. Siles, C. Chen, and J. M. Jornet, "Thz technology for space communications," in *Proc. of the Asia-Pacific Microwave Conference*, 2018.